

# Meson cloud contributions to the Dalitz decays of decuplet to octet baryons

G. Ramalho<sup>1</sup> and K. Tsushima<sup>2</sup>

<sup>1</sup>*Department of Physics and OMEG Institute, Soongsil University, Seoul 06978, Republic of Korea and*

<sup>2</sup>*Laboratório de Física Teórica e Computacional – LFTC, Universidade Cidade de São Paulo, 01506-000, São Paulo, SP, Brazil*

(Dated: December 25, 2023)

We study the role of the meson cloud on the electromagnetic transitions from decuplet ( $B'$ ) to octet ( $B$ ) baryons in terms of the squared four-momentum transfer  $q^2$ . In the quark model framework, the meson cloud dressing of the quark cores gives important contributions to the  $\gamma^*N \rightarrow \Delta(1232)$  transition form factors. In the present work, we estimate the meson cloud contributions of all decuplet to octet baryon transitions ( $\gamma^*B \rightarrow B'$  or  $B' \rightarrow \gamma^*B$ ). Models that combine valence quark effects with pion and kaon cloud dressing provide a fair description of the radiative decays of decuplet to octet baryons, namely the  $\Sigma^0(1385) \rightarrow \gamma\Lambda(1116)$  and  $\Sigma^+(1385) \rightarrow \gamma\Sigma^+(1193)$  decays. Previous studies indicated the relevance of the pion cloud effects on the  $B' \rightarrow \gamma^*B$  transition but also suggested that the kaon cloud contributions may be important in the timelike region. We combine then the contributions of the bare core, estimated by a covariant quark model, with  $q^2$ -dependent contributions of pion and kaon clouds. We use the framework to calculate the Dalitz decay rates and the Dalitz decay widths of decuplet baryons in octet baryons with di-electrons ( $B' \rightarrow e^+e^-B$ ) or di-muons ( $B' \rightarrow \mu^+\mu^-B$ ). We conclude, based on the magnitude of our results, that most estimates of the  $B' \rightarrow e^+e^-B$  Dalitz decay widths may be tested at HADES and PANDA (GSI) in a near future. We discuss also the possibility of measuring the  $\Delta(1232) \rightarrow \mu^+\mu^-N$  and  $\Sigma^0(1385) \rightarrow \mu^+\mu^-\Lambda(1116)$  decay widths in some facilities, based on the estimated branching ratios.

## I. INTRODUCTION

In the last decades there was a significant progress in the study of the electromagnetic structure of baryons using electron-baryon scattering ( $eB \rightarrow eB'$ ) experiments, where  $B$  and  $B'$  are baryons. In these experiments, the baryon target is probed by a spacelike photon ( $\gamma^*B \rightarrow B'$ ), allowing the measurement of transition form factors in terms of  $Q^2 \geq 0$ , where  $Q^2 = -q^2$  and  $q$ , the four-momentum transfer [1–3]. These studies are presently restricted to nucleon ( $N$ ) targets and nucleon excitations ( $N^*$ ) in the final state ( $\gamma^*N \rightarrow N^*$  transition) [1–6]. Unfortunately, the electron-nucleon scattering method cannot be extended from nucleons to other baryons due to the short lifetime of the baryon states [1, 7, 8].

The study of the  $\gamma^*B \rightarrow B'$  transition with timelike photons ( $Q^2 < 0$ ) is more complex experimentally, but can be accessed through the decay  $B' \rightarrow \gamma^*B$ , where the photon is identified by the decay into a dilepton pair ( $\ell^+\ell^-$ ), where  $\ell = e, \mu$  (electron or muon) [9–15]. The state  $B'$  can be generated by scattering of mesons on baryons and by proton-proton or proton-nuclei scattering [7, 9, 16–18]. The reaction  $B' \rightarrow \ell^+\ell^-B$  defines the Dalitz decay of the baryon  $B'$  into the baryon  $B$  and dileptons. Different from the traditional electron-nucleon scattering, at HADES and PANDA, one can probe the electromagnetic structure of the baryons in the kinematic region  $4m_\ell^2 \leq q^2 \leq (M_{B'} - M_B)^2$ , where  $M_{B'}$  and  $M_B$  are

respectively the initial and final baryon masses, and  $m_\ell$  is the mass of the electron or the muon [12, 13, 19]. The baryon dilepton decays provide then information about the electromagnetic structure of the baryons in the timelike region ( $Q^2 = -q^2 < 0$ ) [7, 9–15, 19, 20]. Experiments in the timelike region allow also the possibility of studying the electromagnetic structure of baryons with strange quarks (hyperons) [10, 15, 19].

In the present work, we restrict our study to *direct* electromagnetic decays, excluding weak radiative decays that involve weak transitions (decay of strange quarks) before the final electromagnetic decay. Examples of these processes are the observed decays  $\Lambda \rightarrow \gamma n$ ,  $\Sigma^+ \rightarrow \gamma p$ ,  $\Xi^0 \rightarrow \gamma\Lambda$  and  $\Xi^- \rightarrow \gamma\Sigma^-$ , as well as the Dalitz decays  $\Sigma^+ \rightarrow \mu^+\mu^-p$  and  $\Xi^0 \rightarrow e^+e^-\Lambda$  [21].

The first measured Dalitz decay width of a nucleon resonance, the  $\Delta(1232)$  decay into di-electrons was performed recently at HADES [9, 14, 22, 23]. Measurements of Dalitz decays of other nucleon resonances are in progress at HADES [11–13, 16, 24–27]. Recent feasibility studies on HADES indicate that measurements of hyperon Dalitz decay rates, including  $\Sigma(1385)$ ,  $\Lambda(1404)$  and  $\Lambda(1520)$  into electron-positron pairs are expected at GSI in a near future [10, 18, 19, 28, 29]. The production of hyperons are possible at HADES and PANDA due to the large acceptance and excellent particle identification, including dileptons in the final state [19, 30–32]. There is also the expectation that measurements of baryon Dalitz decays into di-electrons and di-muons may be observed in PANDA, BESIII and LHCb experiments in the following

years [10, 33–36].

It is worth mentioning that the information about radiative decays of baryons is very scarce. The known decays of the decuplet baryons are restricted to a pair of cases:  $\Sigma^0(1385) \rightarrow \gamma\Lambda(1116)$  and  $\Sigma^+(1385) \rightarrow \gamma\Sigma^+(1193)$  decays, apart from the  $\Delta(1232) \rightarrow \gamma^*N$  decays [10, 15, 37]. It is then important to develop theoretical models which may be used to interpret the future experiments in the timelike region and measurements of baryon Dalitz decay rates and widths. At the moment, there are only a few models available for baryon transitions in the timelike region [26, 36, 38–47].

The present work is dedicated to the theoretical study of the  $B' \rightarrow \ell^+\ell^-B$  decays, where  $B'$  is a baryon decuplet member and  $B$  is a baryon octet member. Our calculations are based on the covariant spectator quark model [48–50], where the contribution of the quark core is complemented with an  $SU(3)$  contribution from the pion and kaon clouds, extending previous calculations where the kaon cloud was omitted [15]. The inclusion of the kaon cloud is motivated by estimates of the radiative decays, where it was shown that kaon cloud effects provide significant contributions to the  $\Sigma^0(1385) \rightarrow \gamma\Lambda(1116)$ ,  $\Sigma(1385) \rightarrow \gamma\Sigma(1193)$ , and  $\Xi(1530) \rightarrow \gamma\Xi(1318)$  decays [37]. We start our study analyzing the Dalitz decays into di-electrons ( $B' \rightarrow e^+e^-B$ ), since they are favored kinematically. At the end, we make also predictions for the  $B' \rightarrow \mu^+\mu^-B$  decays. Our analytic expressions are compared with expressions derived within the  $U$ -spin,  $SU(3)$  and  $SU(6)$  symmetries.

Concerning the theoretical study of the octet baryon to the octet baryon transitions in the spacelike region, including the photon point ( $q^2 = 0$ ), there are studies based on a multitude of frameworks, including nonrelativistic and relativistic quark models [51–56], Dyson-Schwinger equations [57], lattice QCD simulations [58, 59], QCD sum rules [60, 61], Skyrme and soliton models [62, 63],  $SU(3)$  flavor models [36, 64, 65], chiral perturbation theory and large- $N_c$  models [66–68]. In general estimates solely on quark models underestimate the data. The estimates get closer to the data when the meson cloud excitations of the bare cores are taken into account [15, 37].

The covariant spectator quark model has been used in the study of the electromagnetic structure of nucleon resonances ( $\gamma^*N \rightarrow N^*$ ), as well as elastic ( $\gamma^*B \rightarrow B$ ) and inelastic ( $\gamma^*B \rightarrow B'$ ) transitions between the baryon states. The described nucleon resonances include the states  $\Delta(1232)$ ,  $N(1440)$ ,  $N(1520)$ ,  $N(1535)$ ,  $\Delta(1600)$ ,  $\Delta(1620)$ ,  $N(1650)$ ,  $N(1700)$  and  $\Delta(1700)$ , among others [50, 69–72]. As for hyperons, the model has been applied to the octet baryons, the decuplet baryons, transitions between the octet and decuplet baryons, the decays of some hyperons [49, 73–78] and  $e^+e^- \rightarrow B\bar{B}$  reactions [79, 80]. The model has also been used in the studies of nucleon deep inelastic scattering [48, 81] and of the electromagnetic and axial structure of baryons in vacuum and in a nuclear medium [75, 82]. The framework provides an alternative to valence quark models because

it takes into account also meson cloud excitations of the baryon cores [37, 74–76]. The model for the octet baryon ( $B$ ) to decuplet baryon ( $B'$ ) transition [37, 76] is here extended to the timelike region following Ref. [15], with minor modifications. The  $B' \rightarrow \gamma^*B$  transitions can be regarded a modification of the  $\Delta(1232) \rightarrow \gamma^*N$  transition, by the quark flavor content of the baryon states. As for the nucleon and  $\Delta(1232)$  systems, we assume that the octet and the decuplet baryon states are dominated by the  $S$ -state quark-diquark components, as will be discussed in the following sections. The valence and meson cloud contributions to the transition form factors are analytically extended to the timelike region, using the magnetic dipole form factor in terms of  $q^2$  and the  $\gamma^*B$  invariant mass  $W$ . The results are then used to determine the Dalitz decay rates and Dalitz decay widths associated with all the decuplet baryon states. The dependence in terms of running mass  $W$ , which may differ from the mass of the pole ( $M_{B'}$ ) is important, because the measurements in the timelike region are performed in terms of the  $\gamma^*B$  invariant mass, and the determination of the Dalitz decay width requires the integration of functions near the pole ( $W = M_{B'}$ ) [9].

We conclude at the end that, the kaon cloud contributions increase about 30%–40% the  $\Sigma(1385)$  to  $\Sigma(1193)$  Dalitz decays, and about 50%–70% the  $\Xi(1530)$  to  $\Xi(1318)$  Dalitz decays. We infer also that the kaon cloud effects are particularly important for the  $\Sigma^0(1385) \rightarrow e^+e^-\Lambda(1116)$  decay, because the kaon cloud contribution is enhanced in the diagram where the photon interacts directly with the intermediate baryon core [diagram (b) in Fig. 1]. As a consequence, the contribution to the Dalitz decay width increases in about 27%, improving significantly the estimates which include only pion cloud effects. We conclude also that, measurements of the  $\Sigma^+(1385) \rightarrow e^+e^-\Sigma^+(1193)$ ,  $\Sigma^0(1385) \rightarrow e^+e^-\Sigma^0(1193)$ ,  $\Xi^0(1530) \rightarrow e^+e^-\Xi^0(1318)$  and  $\Xi^-(1530) \rightarrow e^+e^-\Xi^-(1318)$  decay widths may be expected to be measured in a near future at HADES and PANDA [10]. Based on our estimates of the branching ratios and the experimental limits, we can also expect to observe the  $\Delta(1232) \rightarrow \mu^+\mu^-N$  and  $\Sigma^0(1385) \rightarrow \mu^+\mu^-\Lambda(1116)$  decays at BESIII and LHCb in the near future [34, 35].

The present work is organized as follows: in the next section, we present the formalism associated with the radiative and Dalitz decays of decuplet baryons into octet baryons. The formalism of the covariant spectator quark model is presented in Sec. III, while the expressions associated with the bare valence quark and meson cloud contributions are discussed in Secs. IV and V, respectively. In Sec. VI, we present our numerical results for the transition form factors in terms of  $q^2$ . The estimates of the radiative decays, the Dalitz decay rates and the Dalitz decay widths into di-electron and di-muon pairs are presented and discussed in Sec. VII. The outlook and conclusions are given in Sec. VIII. Additional information is also given in Appendixes A to D.

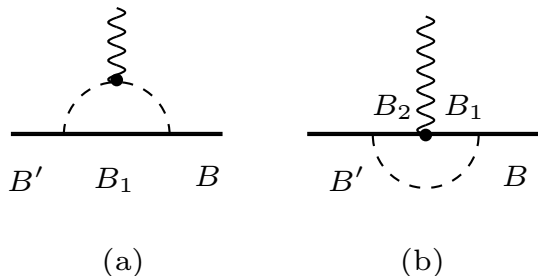


FIG. 1. Meson cloud contributions for the electromagnetic transition form factors. Between the initial octet ( $B$ ) and final decuplet ( $B'$ ) baryon states, there are several possible intermediate baryon states:  $B_1$  in diagram (a);  $B_1$  and  $B_2$  in diagram (b).

## II. RADIATIVE AND DALITZ DECAY OF DECUPLER BARYONS INTO OCTET BARYONS

In this section we discuss the formalism associated with the analysis of the radiative ( $B' \rightarrow \gamma B$ ) and Dalitz dilepton ( $B' \rightarrow \ell^+ \ell^- B$ ) decays of a decuplet baryon member  $B'$  into an octet baryon member  $B$ . The formalism described below is valid in general for  $\frac{3}{2}^+ \rightarrow \frac{1}{2}^+$  baryon transitions, using the notation  $J^P$ , where  $J$  represent the spin and  $P$  the parity. As before,  $M_{B'}$  and  $M_B$  represent the mass of  $B'$  and  $B$ , respectively.

We start with the Dalitz decay into di-electrons ( $\ell = e$ ). In the following we use the indices  $\gamma^* B$ ,  $e^+ e^- B$  and  $\gamma B$  to describe the decays  $B' \rightarrow \gamma^* B$ ,  $B' \rightarrow e^+ e^- B$ , and  $B' \rightarrow \gamma B$ , in that order, when the baryon  $B'$  is well identified. Later on we discuss the Dalitz di-muon decays ( $\ell = \mu$ ).

The Dalitz decay  $B' \rightarrow e^+ e^- B$  depends on the invariant squared four-momentum  $q^2$  of the di-electron pair ( $e^+ e^-$ ), and it is then limited by the  $q^2 \geq 4m_e^2 > 0$ , where  $m_e$  is the electron mass. The determination of the Dalitz decay width requires the use of the function  $\Gamma_{\gamma^* B}(q, W)$ , where  $W$  is the energy associated with the  $\gamma^* N$  state and  $q = \sqrt{q^2}$ . The Dalitz decay is interpreted as a consequence of a decay of a virtual timelike photon into a pair of electrons ( $\gamma^* \rightarrow e^+ e^-$ ).

Notice that, in the timelike region, we replace the dependence on the mass  $M_{B'}$  by  $W$ , in order to extend the discussion of the cases where the  $\gamma^* B$  invariant energy does not correspond to the pole  $M_{B'}$ .

The function  $\Gamma_{\gamma^* B}(q, W)$  is determined by [10, 14, 22, 23, 83]

$$\Gamma_{\gamma^* B}(q, W) = \frac{\alpha}{16} \frac{(W + M_B)^2}{W^3 M_B^2} \sqrt{y_+ y_-} |G_T(q^2, W)|^2, \quad (2.1)$$

where  $\alpha \simeq 1/137$  is the fine-structure constant, and

$$y_{\pm} = \sqrt{(W \pm M_B)^2 - q^2}. \quad (2.2)$$

The function  $|G_T(q^2, W)|^2$  takes the form

$$|G_T(q^2, W)|^2 = |G_M(q^2, W)|^2 + |G_E(q^2, W)|^2 + \frac{q^2}{2W^2} |G_C(q^2, W)|^2, \quad (2.3)$$

where  $G_M$ ,  $G_E$  and  $G_C$  are respectively the magnetic dipole, the electric quadrupole and the Coulomb quadrupole  $\gamma^* B \rightarrow B'$  transition form factors, as defined by Jones and Scadron [84, 85].

The Dalitz decay width  $\Gamma_{e^+ e^-}(W)$  is determined by the integral,

$$\Gamma_{e^+ e^- B}(W) = \int_{2m_e}^{W - M_B} \Gamma'_{e^+ e^- B}(q, W) dq, \quad (2.4)$$

where

$$\Gamma'_{e^+ e^- B}(q, W) \equiv \frac{d\Gamma_{e^+ e^- B}(q, W)}{dq}, \quad (2.5)$$

represents the Dalitz decay rate function.

The function  $\Gamma'_{e^+ e^- B}$  can be evaluated using [9, 10, 14, 23, 86]

$$\Gamma'_{e^+ e^- B}(q, W) = \frac{2\alpha}{3\pi q} \Gamma_{\gamma^* B}(q, W). \quad (2.6)$$

Notice in Eq. (2.4), that the integration in  $q$  is limited to the physical region  $4m_e^2 \leq q^2 \leq (W - M_B)^2$ , where the momenta of the baryons  $B'$  and  $B$  are well defined. The upper limit corresponds to the limit where the photon three-momentum vanishes ( $\mathbf{q} = \mathbf{0}$ ). In that limit the functions  $G_E$  and  $G_C$  are correlated and  $G_M$  is finite [22, 84, 87–89].

The radiative decay width is defined by the function  $\Gamma_{\gamma^* B}$ , from Eq. (2.1), when  $q^2 = 0$  [23, 86],

$$\Gamma_{\gamma B}(W) \equiv \Gamma_{\gamma^* B}(0, W). \quad (2.7)$$

The baryon  $B'$  radiative decay ( $B' \rightarrow \gamma B$ ) measured in the experiments, corresponds to the result from Eq. (2.1) in the limits  $W = M_{B'}$  and  $q^2 = 0$ ,

$$\Gamma_{\gamma B} \equiv \Gamma_{\gamma B}(M_{B'}) = \Gamma_{\gamma^* B}(0, M_{B'}). \quad (2.8)$$

From the formalism discussed above, we conclude that the key ingredient to the calculation of the Dalitz decay widths and the radiative decay widths is the determination of the transition form factors in the regime  $q^2 \geq 0$ . Once one has a model for the transition form factors for  $q^2 \geq 0$  in terms of a running mass  $W$ , we can calculate  $|G_T(q^2, W)|$ , and consequently  $\Gamma_{\gamma B}(W)$ , the Dalitz decay rate  $\Gamma'_{e^+ e^- B}(q, W)$ , and the Dalitz decay width  $\Gamma_{e^+ e^- B}(W)$ .

An important aspect of the octet baryon to decuplet baryon electromagnetic transitions is that the magnetic dipole form factor is the dominant contribution to  $|G_T(q^2, W)|$ . Taking the  $\gamma^* N \rightarrow \Delta(1232)$  transition as an example, it is known that near  $q^2 = 0$ ,  $G_E$

is about 3–5% of  $G_M$  [88, 89]. In these conditions  $G_E$  can be neglected in a first approximation. As for  $G_C$ , the magnitude near  $q^2 = 0$  is larger and can be estimated using Siegert's theorem as  $G_C = \frac{2M_\Delta}{M_\Delta - M_N} G_E \simeq (0.03 - 0.05) \frac{2M_\Delta}{M_\Delta - M_N} G_M$ , or 25–42% of  $G_M$  [88]. Notice, however, that the  $G_C$  contribution to  $|G_T|^2$  is suppressed kinematically by the factor  $q^2/(2M_\Delta^2)$ . An estimate based on the relation between  $G_E$  and  $G_C$  near  $q^2 = (M_\Delta - M_N)^2 \simeq 0.086 \text{ GeV}^2$ , indicates that the term in  $|G_C|^2$  contribute to  $|G_T|^2$  with about  $2|G_E|^2$ .<sup>1</sup> The combination of the quadrupole form factors to  $|G_T|^2$  can then be estimated as  $3|G_E|^2$  in the region between  $q^2 = 0$  and  $(M_\Delta - M_N)^2$ . From the ratio  $|G_E|/|G_M| \simeq 0.03 - 0.05$ , we can conclude that  $|G_T|^2 \simeq |G_M|^2$ , apart the corrections of 0.3–0.8%. The conclusion is then that in the Dalitz decay, the dominance of the magnetic dipole form factor is a good approximation.

Using the dominance of magnetic dipole form factor ( $G_E = G_C \simeq 0$ ) we can replace in Eq. (2.1),  $|G_T|^2$  by  $|G_M|^2$ . The radiative decay width (2.8) can also be reduced to

$$\Gamma_{\gamma B} = \frac{\alpha}{16} \frac{(M_{B'}^2 - M_B^2)^3}{M_{B'}^3 M_B^2} |G_M(0, M_{B'})|^2. \quad (2.9)$$

For the description of the Dalitz decay into a pair of muons, we consider the expression [83]

$$\Gamma'_{\mu^+\mu^-B}(q, W) = \frac{2\alpha}{3\pi q} C_\mu(q^2) \Gamma_{\gamma^*B}(q, W), \quad (2.10)$$

where

$$C_\mu(q^2) = \left(1 + \frac{2\mu^2}{q^2}\right) \sqrt{1 - \frac{4\mu^2}{q^2}}, \quad (2.11)$$

and  $\mu$  is mass of the muon. A similar factor, with  $\mu$  replaced by  $m_e$  should also be included in the case of the di-electron decay in Eq. (2.6). In that case, however, one can use  $C_e \simeq 1$ , since the electron mass is negligible in the comparison with the other scales.

The Dalitz decay width  $\Gamma_{\mu^+\mu^-B}(W)$  is calculated similarly to  $\Gamma_{e^+e^-B}(W)$  from Eq. (2.4)

$$\Gamma_{\mu^+\mu^-B}(W) = \int_{2\mu}^{W-M_B} \Gamma'_{\mu^+\mu^-B}(q, W) dq, \quad (2.12)$$

where the limits of integration are redefined according to the value of the muon mass.

From the reduction of the integration interval, from  $[2m_e, W - M_B]$  to  $[2\mu, W - M_B]$ , and the weight function

$C_\mu \leq 1$ , one can anticipate that the di-muon Dalitz decay width is smaller than the di-electron decay width. Notice also that the function  $C_\mu$  reduces strongly the function  $\Gamma'_{\mu^+\mu^-B}(q, W)$  in the threshold of the integration ( $q = 2\mu$ ).

### III. COVARIANT SPECTATOR QUARK MODEL

We discuss now the formalism used in the present work in the calculations of the  $\gamma^*B \rightarrow B'$  transition form factors, based on the covariant spectator quark model. The details are discussed in the next two sections.

The covariant spectator quark model is a constituent quark model derived from the covariant spectator theory [48, 50, 90]. Within the framework, the baryons are described as three-constituent quark systems, where a quark is free to interact with electromagnetic fields in impulse approximation. The electromagnetic interaction with the quarks is described in terms of quark form factors, that simulate the structure associated with the gluon and quark-antiquark dressing of the quarks. The constituent quark form factors are parametrized using a vector meson dominance (VMD) structure calibrated in the study of the electromagnetic structure of the nucleon and baryon decuplet [48, 49].

When we consider the electromagnetic interaction in the covariant spectator theory, we can integrate over the quark-pair degrees of freedom, since they are spectators in the interaction, and reduce the system to a diquark-quark state, where the diquark can be represented as an on-mass-shell particle with effective mass  $m_D$  [48, 91]. The baryon wave functions are derived from spin-flavor-radial symmetries associated with the diquark-quark configurations. The baryon states with quantum numbers  $\frac{1}{2}^+$  and  $\frac{3}{2}^+$  can be represented as combinations of  $S$  and  $D$  states [48, 69, 70, 73, 91]. The radial wave functions are determined phenomenologically by experimental data, or lattice QCD results for some ground state systems [48–50, 70, 71, 74].

The  $\Delta(1232) \rightarrow \gamma^*N$  transition in particular, can be interpreted, as in nonrelativistic quark models, as dominated by the flip of the spin of a quark from the initial state (spin 1/2) to the final state (spin 3/2), which can justify the dominance of the transition by the magnetic dipole form factor  $G_M$  [1, 3, 4, 50, 69–71, 92]. Small corrections, including angular momentum excitations can induce small contributions to the electric ( $G_E$ ) quadrupole form factor and to  $\frac{|q|}{2M_\Delta} G_C$ , where  $G_C$  is the Coulomb quadrupole form factor. The non-zero results for these functions are interpreted as a manifestation of the  $\Delta(1232)$  deformation [58, 70, 73, 92–97]. We notice, however, as discussed in the previous section that, the measured magnitudes of the electric ( $G_E$ ) and Coulomb ( $G_C$ ) quadrupole form factors provide only small contributions to the function  $G_T(q^2, M_\Delta)$  near  $q^2 = 0$ , and that in practice we can use the approximation  $|G_T| \simeq |G_M|$ .

<sup>1</sup> According to Siegert's theorem,  $G_E = \frac{M_\Delta - M_N}{2M_\Delta} G_C$  near the pseudothreshold  $q^2 = (M_\Delta - M_N)^2$  [87–89]. Since this point is very close to  $q^2 = 0$ , we can use the relation to estimate  $\frac{q^2}{2W^2} |G_C|^2$ , when  $W$  is close to  $M_\Delta$ . We obtain then  $\frac{q^2}{2W^2} |G_C|^2 = \frac{(W - M_N)^2}{2W^2} |G_C|^2 \simeq 2|G_E|^2$ .

We conclude then, as discussed extensively in the literature, that the  $\Delta(1232) \rightarrow \gamma^* N$  transition is dominated by the magnetic dipole form factor [1, 3, 5, 70, 71, 88].

It is important also to mention that the calculations based on the three-quark wave functions are not the full story, and that other effects have to be taken into account if we want to describe  $\gamma^* B \rightarrow B'$  transition for arbitrary baryon states,  $B$  and  $B'$ . Even though our quarks have structure, including meson cloud or quark-antiquark dressing of the quarks, there are processes involving the meson cloud dressing that are not taken explicitly into account. The processes in which there is a meson exchange between the different quarks inside the baryons cannot be represented by the quark dressing due to the meson cloud. These processes are regarded in our formalism, as a meson emitted by a baryon state and absorbed by another baryon state, based on a baryon-meson molecular picture [14, 37, 50, 76]. The importance of the effect of the meson cloud dressing has been discussed in different frameworks and emphasizes the importance of the interplay between quark models and dynamical baryon-meson reaction models, where the baryon-meson interaction is taken into account explicitly [3, 93, 98].

The corollary of the previous discussion is that in the calculation of transition form factors, one needs to take into account the contributions of the valence quark core and the contributions of the meson cloud, which surrounds the baryon cores. Considering now the octet baryon to decuplet baryon electromagnetic transitions ( $\gamma^* B \rightarrow B'$ ), we assume that similarly to the  $\gamma^* N \rightarrow \Delta(1232)$  transition, those transitions are dominated by the magnetic dipole form factors, since the  $S$ -wave components of the wave functions are also dominant. In these conditions, we can use the decomposition [2, 14, 15, 37, 69, 70],

$$G_M(q^2, W) = G_M^B(q^2, W) + G_M^{MC}(q^2, W), \quad (3.1)$$

where B labels the contribution of the valence quark core (bare contribution) and MC labels the contribution associated with the meson cloud dressing.

The expressions for  $G_M^B(q^2, W)$  and  $G_M^{MC}(q^2, W)$  are discussed in Secs. IV and V, respectively. In Eq. (3.1),  $G_M^B(q^2, W)$  and  $G_M^{MC}(q^2, W)$  have different falloffs for very large  $|q^2|$ . The dominant valence quark contribution follows  $G_M^B(q^2, W) \propto 1/q^4$ , as expected from a perturbative QCD (pQCD) analysis [99, 100]. The meson cloud contributions fall off more quickly, with  $G_M^{MC}(q^2, W) \propto 1/q^8$ , as will be discussed in Sec. V.

The meson cloud contributions for the  $\gamma^* B \rightarrow B'$  transitions are dominated near  $q^2 = 0$  by the pion and kaon clouds and have significant contributions to the radiative decay widths [37]. The pion cloud contributions for the Dalitz di-electron decays were studied in a previous work [15]. In the present work, we extend the model with the explicit inclusion of the kaon cloud effects. In the following sections, we present a summary of the formalism, and refer the reader to the appendixes and to Ref. [15]

## IV. VALENCE QUARK CONTRIBUTIONS

We consider now the contribution from the valence quarks to the  $\gamma^* B \rightarrow B'$  transition. We use the wave functions associated with the decuplet baryon member  $\Psi_{B'}(P_+, k)$  and the octet baryon member  $\Psi_B(P_-, k)$ , where  $P_+$  and  $P_-$  are the final and initial baryon momenta, respectively, and  $k$  is the diquark momentum. Recall that the diquark is on-mass-shell in the covariant spectator quark model. The wave functions are expressed into diquark-quark states. For simplicity, we suppress in the wave functions the labels associated with the flavor and spin. As mentioned already, we assume that the octet baryon and the decuplet baryon states are dominated by the diquark-quark  $S$ -wave state. This assumption is consistent with the dominance of the magnetic dipole form factor observed in the  $\gamma^* N \rightarrow \Delta(1232)$  transition. The explicit expressions for  $\Psi_{B'}(P_+, k)$  and  $\Psi_B(P_-, k)$ , in the  $S$ -wave approximation, are presented in Ref. [15].

### A. Transition current

The  $\gamma^* B \rightarrow B'$  transition current in the relativistic impulse approximation takes the form [48, 49, 91]

$$J^\mu = 3 \sum_{\Gamma} \int_k \bar{\Psi}_{B'}(P_+, k) j_q^\mu(q) \Psi_B(P_-, k), \quad (4.1)$$

where  $j_q^\mu$  is the quark current operator, depending on momentum transfer  $q = P_+ - P_-$ , and the wave functions are expressed in terms of diquark-quark states [48, 50, 69]. There is no ambiguity in the notation for  $q$ , because the sub-indexes  $q$  are replaced by  $q = u, d, s$ . The integration symbol represents the covariant integration on the on-mass-shell diquark momentum ( $k$ ), and the sum is over the diquark polarization states, including the scalar and vector components. The factor 3 takes into account the sum in the quarks based on the wave function symmetries.

The quark current  $j_q^\mu$  ( $q = u, d, s$ ) includes the electromagnetic structure of the constituent quarks and can be expressed in the form [48, 49]

$$j_q^\mu(q) = j_1(q^2) \gamma^\mu + j_2(q^2) \frac{i \sigma^{\mu\nu} q_\nu}{2M_N}, \quad (4.2)$$

where  $j_i$  ( $i = 1, 2$ ) are the Dirac and Pauli electromagnetic flavor operators, respectively, and act on the third-quark component of the wave function. In Eq. (4.1)  $M_N$  represents the nucleon mass. Notice that we use here  $q^2 = -Q^2$ , instead of  $Q^2$ , since we are focusing on the timelike kinematics.

The components of the quark current  $j_i$  ( $i = 1, 2$ ) can be decomposed as the sum of operators

$$j_i(q^2) = \frac{1}{6} f_{i+}(q^2) \lambda_0 + \frac{1}{2} f_{i-}(q^2) \lambda_3 + \frac{1}{6} f_{i0}(q^2) \lambda_s, \quad (4.3)$$

where

$$\lambda_0 = \begin{pmatrix} 1 & 0 & 0 \\ 0 & 1 & 0 \\ 0 & 0 & 0 \end{pmatrix}, \quad \lambda_3 = \begin{pmatrix} 1 & 0 & 0 \\ 0 & -1 & 0 \\ 0 & 0 & 0 \end{pmatrix},$$

$$\lambda_s = \begin{pmatrix} 0 & 0 & 0 \\ 0 & 0 & 0 \\ 0 & 0 & -2 \end{pmatrix}, \quad (4.4)$$

are the flavor operators. These operators act on the quark wave function in flavor space,  $q = (u d s)^T$ .

The functions  $f_{i+}$ ,  $f_{i-}$  represent the quark isoscalar and isovector form factors, respectively, based on the combinations of the quarks  $u$  and  $d$ . The functions  $f_{i0}$  represent the structure associated with the strange quark. The isoscalar, isovector and strange quark form factors are parametrized according to a VMD form and are expressed in terms of vector meson mass poles associated with the  $\rho$ ,  $\omega$  and  $\phi$  depending on the type ( $l = \pm, 0$ ). For the mass of  $\rho$ , we use a value determined by a fit to the  $\pi$  electromagnetic form factors, as discussed in the next section. The expressions of the quark form factors are valid for the spacelike and timelike regions. In the timelike region, however, the vector meson mass poles are corrected by finite decay widths. The explicit form for the quark form factors is included in Appendix A.

## B. Transition form factors

The transition form factors are calculated from the transition current given by Eq. (4.1) [69, 76]. When we consider wave functions for the baryons  $B$  and  $B'$ , based on an  $S$ -wave diquark-quark structure, we conclude that only the magnetic dipole form factor contributes ( $G_E = G_C = 0$ ) [69, 70]. The final expression for the valence quark contribution to  $G_M$ ,  $G_M^B$  depends on the ( $S$ -wave) radial wave functions of the decuplet baryon member  $\psi_{B'}(P_+, k)$  and the octet baryon member  $\psi_B(P_-, k)$ . In the covariant spectator quark model formalism, the radial wave function  $\psi_B(P, k)$  of a generic baryon  $B$  can be parametrized in terms of the variable

$$\chi_B = \frac{(M_B - m_B)^2 - (P - k)^2}{M_B m_D}, \quad (4.5)$$

where  $M_B$  and  $m_D$  are the baryon mass and diquark mass, respectively. This parametrization is possible because both the baryon  $B$  and the diquark are on-mass-shell [48].

The explicit expressions for  $\psi_{B'}$  and  $\psi_B$  are presented in Ref. [15]. The parameters associated with the octet and decuplet baryon wave functions were determined in previous works by fits to lattice QCD data [49, 76].

In the following, we replace the mass of the decuplet baryon member  $M_{B'}$  by the  $W$ , according to the discussion of the previous sections.

The final expression for the valence quark contribution to the magnetic dipole form factor is [69, 76]

$$G_M^B(q^2, W) = \frac{4}{3\sqrt{3}} g_v \mathcal{I}(q^2, W), \quad (4.6)$$

where

$$\mathcal{I}(q^2, W) = \int_k \psi_{B'}(P_+, k) \psi_B(P_-, k), \quad (4.7)$$

is the overlap integral of the octet baryon and decuplet baryon radial wave functions (the  $W$  dependence comes from  $\psi_{B'}$ ), and

$$g_v = \frac{1}{\sqrt{2}} \left[ \frac{2M_B}{W + M_B} j_1^S(q^2) + \frac{M_B}{M_N} j_2^S(q^2) \right]. \quad (4.8)$$

The functions  $j_i^S$  ( $i = 1, 2$ ) represent the projection of the flavor operators onto the flavor components of the decuplet baryon and the mixed symmetric component of the octet baryon flavor state [76]. The explicit expressions in terms of the quark form factors, determined by the wave functions  $\Psi_{B'}(P_+, k)$  and  $\Psi_B(P_-, k)$  are presented in the second column of Table I. More details can be found in Ref. [15].

In Table I and along the article, we use the asterisk (\*) to represent the excited states of  $\Sigma$  and  $\Xi$ , members of the baryon decuplet. The label  $\gamma^* N \rightarrow \Delta$  includes the  $\gamma^* p \rightarrow \Delta^+$  and  $\gamma^* n \rightarrow \Delta^0$  transitions ( $p$  is the proton and  $n$  is the neutron).

The octet baryon ( $\psi_B$ ) and decuplet baryon ( $\psi_{B'}$ ) radial wave functions, presented above, ensure that the valence quark contribution to  $G_M$  defined by Eq. (4.6) is proportional to  $1/Q^4$  for very large  $Q^2$  [69], consistent with estimates from perturbative QCD (pQCD) [100].

The use of the present parametrizations for  $G_M^B$  and for the radial wave functions is discussed in detail in our previous work on this subject [15]. Here, we mention only the relevant points. The parametrization for the radial wave functions is justified because those functions are calibrated by lattice QCD data for large pion masses and therefore, there is no significant contamination from meson cloud effects. Due to the nature of the transitions, in addition to the valence quark effects, one needs also to consider the effects associated with the pion and kaon clouds. The present parametrizations, including the meson cloud parametrizations of the next section, are supported by the available data for the octet baryon to decuplet baryon transitions, namely by the  $\gamma^* N \rightarrow \Delta(1232)$  transition. Our parametrization of the  $\Delta(1232)$  radial wave function is consistent with lattice QCD data and with the EBAC/Argonne-Osaka [1, 3, 98] estimates of the bare core contribution to  $G_M$  [14, 22, 37, 69, 70, 76].

## C. $SU(3)$ structure of $G_M^B$

The valence quark contribution to  $G_M$ , determined by Eq. (4.6) carry the  $SU(3)$  symmetry structure through

	$j_i^S(f_{iu})$	$j_i^S(f_{iq})$	$j_i^S(f_{i-}, \Delta_i)$
$\gamma^* N \rightarrow \Delta$	$\sqrt{2}f_{i-}$	$\frac{\sqrt{2}}{3}(2f_{iu} + f_{id})$	$\sqrt{2}f_{i-}$
$\gamma^* \Lambda \rightarrow \Sigma^{*0}$	$\sqrt{\frac{3}{2}}f_{i-}$	$\frac{1}{\sqrt{6}}(2f_{iu} + f_{id})$	$\sqrt{\frac{3}{2}}f_{i-}$
$\gamma^* \Sigma^+ \rightarrow \Sigma^{*+}$	$\frac{\sqrt{2}}{6}(f_{i+} + 3f_{i-} + 2f_{i0})$	$\frac{\sqrt{2}}{3}(2f_{iu} + f_{is})$	$\sqrt{2}f_{i-} - \frac{\sqrt{2}}{3}\Delta_i$
$\gamma^* \Sigma^0 \rightarrow \Sigma^{*0}$	$\frac{\sqrt{2}}{6}(f_{i+} + 2f_{i0})$	$\frac{\sqrt{2}}{6}(2f_{iu} - f_{id} + 2f_{is})$	$\frac{\sqrt{2}}{2}f_{i-} - \frac{\sqrt{2}}{3}\Delta_i$
$\gamma^* \Sigma^- \rightarrow \Sigma^{*-}$	$\frac{\sqrt{2}}{6}(f_{i+} - 3f_{i-} + 2f_{i0})$	$\frac{\sqrt{2}}{3}(-f_{id} + f_{is})$	$-\frac{\sqrt{2}}{3}\Delta_i$
$\gamma^* \Xi^0 \rightarrow \Xi^{*0}$	$\frac{\sqrt{2}}{6}(f_{i+} + 3f_{i-} + 2f_{i0})$	$\frac{\sqrt{2}}{3}(2f_{iu} + f_{is})$	$\sqrt{2}f_{i-} - \frac{\sqrt{2}}{3}\Delta_i$
$\gamma^* \Xi^- \rightarrow \Xi^{*-}$	$\frac{\sqrt{2}}{6}(f_{i+} - 3f_{i-} + 2f_{i0})$	$\frac{\sqrt{2}}{3}(-f_{id} + f_{is})$	$-\frac{\sqrt{2}}{3}\Delta_i$

TABLE I. Coefficients  $j_i^S$  ( $i = 1, 2$ ) used to calculate the valence quark contributions for the transition form factors using different representations ( $l = \pm, 0$  and  $q = u, d, s$ ). The label  $\gamma^* N \rightarrow \Delta$  includes the  $\gamma^* p \rightarrow \Delta^+$  and  $\gamma^* n \rightarrow \Delta^0$  transitions ( $p$  is the proton and  $n$  is the neutron).  $\Delta_i = f_{id} - f_{is}$ .

the coefficients  $j_i^S$ . The  $\gamma^* N \rightarrow \Delta$  and  $\gamma^* \Lambda \rightarrow \Sigma^{*0}$  transitions have a pseudovector character. The coefficients  $j_i^S$  are zero ( $\gamma^* \Sigma^- \rightarrow \Sigma^{*-}$  and  $\gamma^* \Xi^- \rightarrow \Xi^{*-}$ ) or functions proportional to  $f_{i-}$  in the limit  $f_{i+} \equiv f_{i-} \equiv f_{i0}$  [exact  $SU(3)$  symmetry limit]. The expressions for  $G_M^B$  are reduced to five non-zero functions which differ from the result for  $\gamma^* N \rightarrow \Delta$  by a single coefficient (1,  $1/\sqrt{3}$ , 1,  $1/2$ , 0, 1, 0) in the limit where all members of the octet have the mass  $M_B$  and all members of the decuplet have the mass  $W$ .

The conclusion is then that, in the exact  $SU(3)$  symmetry limit, all non-zero transitions are determined by a single function, which we can choose as the result for the  $\gamma^* N \rightarrow \Delta$  transition. Next, we consider a weaker restriction of the  $SU(3)$  symmetry, the  $U$ -spin symmetry.

#### D. $U$ -spin symmetry

For the following discussion, it is convenient to replace the representation of the isoscalar, isovector and  $f_{i0}$  quark form factors by the  $u$ ,  $d$ , and  $s$  quark form factors. For the conversion, we use the relations ( $i = 1, 2$ ) [48, 49]

$$+\frac{2}{3}f_{iu} = \frac{1}{6}f_{i+} + \frac{1}{2}f_{i-}, \quad (4.9)$$

$$-\frac{1}{3}f_{id} = \frac{1}{6}f_{i+} - \frac{1}{2}f_{i-}, \quad (4.10)$$

$$-\frac{1}{3}f_{is} = -\frac{1}{3}f_{i0}. \quad (4.11)$$

The pre-factors  $e_q = -\frac{1}{3}, +\frac{2}{3}$  are related to the charges of the quarks  $u$  ( $+\frac{2}{3}$ ) and  $d, s$  ( $-\frac{1}{3}$ ).

A useful relation is

$$3f_{i-} = 2f_{iu} + f_{id}. \quad (4.12)$$

The expressions for  $j_i^S$  in terms of the quark form factors  $f_{iq}$  are presented in the third column of Table I.

The valence quark contributions to the transition form factors can also be estimated within the  $U$ -spin symmetry [64, 101]. In the  $U$ -spin symmetry one can replace a  $s$  quark by a  $d$  quark in the initial and final baryon states. The  $U$ -spin symmetry is exact when we can replace the  $f_{id}$  by  $f_{is}$ .

Using the notation from Eqs. (4.9)–(4.11) and

$$\Delta_i = f_{id} - f_{is}, \quad (4.13)$$

we obtain the expressions for  $j_i^S$  presented in the fourth column of Table I.

The effect of the  $U$ -spin can be seen more clearly in the last column of Table I. The factor associated with  $\gamma^* \Sigma^- \rightarrow \Sigma^{*-}$  and  $\gamma^* \Xi^- \rightarrow \Xi^{*-}$  vanish in the limit  $\Delta_i = 0$  (or  $f_{id} \equiv f_{is}$ ), and all the other coefficients became proportional to  $f_{i-}$  (quark isovector form factor).

Additional relations can now be derived for the transition form factors, when we assume that all octet baryon members have the same mass, and all decuplet baryon members have the same mass. In that case, we can write:

$$G_M(\gamma^* \Lambda \rightarrow \Sigma^{*0}) = \frac{\sqrt{3}}{2}G_M(\gamma^* n \rightarrow \Delta^0), \quad (4.14)$$

$$G_M(\gamma^* \Sigma^+ \rightarrow \Sigma^{*+}) = G_M(\gamma^* p \rightarrow \Delta^+), \quad (4.15)$$

$$G_M(\gamma^* \Xi^0 \rightarrow \Xi^{*0}) = \frac{1}{2}G_M(\gamma^* \Sigma^0 \rightarrow \Sigma^{*0}), \quad (4.16)$$

$$G_M(\gamma^* \Sigma^- \rightarrow \Sigma^{*-}) = G_M(\gamma^* \Xi^- \rightarrow \Xi^{*-}) \equiv 0. \quad (4.17)$$

The novelty of the above relations compared with most of the  $U$ -spin analysis is the direct relation between the  $\gamma^* \Xi^0 \rightarrow \Xi^{*0}$  and  $\gamma^* \Sigma^0 \rightarrow \Sigma^{*0}$  transitions. Using the  $\gamma^* N \rightarrow \Delta$  transition as reference,

$$G_M^0 \equiv G_M(\gamma^* N \rightarrow \Delta), \quad (4.18)$$

we can express all the non-zero form factors as

$$G_M(\gamma^* N \rightarrow \Delta) = G_M^0, \quad (4.19)$$

$$G_M(\gamma^* \Lambda \rightarrow \Sigma^{*0}) = \frac{\sqrt{3}}{2} G_M^0, \quad (4.20)$$

$$G_M(\gamma^* \Sigma^+ \rightarrow \Sigma^{*+}) = G_M^0, \quad (4.21)$$

$$G_M(\gamma^* \Sigma^0 \rightarrow \Sigma^{*0}) = \frac{1}{2} G_M^0, \quad (4.22)$$

$$G_M(\gamma^* \Xi^0 \rightarrow \Xi^{*0}) = G_M^0. \quad (4.23)$$

The previous relations can help to understand the relative magnitude of the different radiative decay widths. These relations, however, are not precise enough to estimate the final results, for the following three main reasons: (i) the meson cloud effects are relevant and change the magnitude of  $G_M$ ; (ii) the amount of meson cloud varies from decay to decay; and (iii) the coefficient of  $|G_M(0)|^2$  involved in the calculations of  $\Gamma_{\gamma B}$  depends on the baryon masses. The last effect is a consequence of the  $SU(3)$  symmetry breaking.

A consequence of the mass factor is that  $\Gamma_{\Sigma^{*+} \rightarrow \gamma \Sigma^+} \simeq \Gamma_{\Delta \rightarrow \gamma N}$  and  $\Gamma_{\Sigma^{*0} \rightarrow \gamma \Sigma^0} \simeq \frac{1}{4} \Gamma_{\Delta \rightarrow \gamma N}$  are not good approximations. In contrast,  $\Gamma_{\Sigma^{*0} \rightarrow \gamma \Lambda} \simeq \frac{3}{4} \Gamma_{\Delta \rightarrow \gamma N}$  and  $\Gamma_{\Sigma^{*0} \rightarrow \gamma \Sigma^0} \simeq \frac{1}{4} \Gamma_{\Sigma^{*+} \rightarrow \gamma \Sigma^+}$  provide good estimates, because the mass factors are similar and the meson cloud contributions have similar proportions.

## V. MESON CLOUD CONTRIBUTIONS

The pion cloud contributions to the  $\gamma^* B' \rightarrow B$  transitions are estimated by the  $SU(3)$  extension of our pion cloud model for the  $\gamma^* N \rightarrow \Delta(1232)$  transition [69–71].

We use in particular the results of Ref. [37], where the meson cloud contributions of the diagrams of Fig. 1 are determined explicitly in the limit  $q^2 = 0$ . The calculations of the meson cloud loops are based on the cloudy bag model (CBM) [102–107]. More calculations of  $\gamma^* N \rightarrow \Delta(1232)$  transition form factors based on the CBM can be found in Refs. [108–110].

The explicit calculations use the meson-baryon couplings for the possible octet baryon and decuplet baryon intermediate states from Fig. 1. The connection with the quark microscopic properties between the covariant spectator quark model and the CBM is performed matching the Dirac and Pauli couplings. The expressions used for the calculations of the meson cloud contributions are presented in Appendixes B, C, and D. In addition to the pion, we consider also the contributions of the  $K^-$ ,  $\bar{K}^-$  and  $\eta$ -meson cloud contributions [37]. The  $\eta$ -meson cloud contributions prove to be very small.

We describe next how to generalize the pion and kaon ( $K$  and  $\bar{K}$ ) cloud contributions to finite  $q^2$ .

## A. Pion cloud contributions

The calculation of the pion cloud contributions to the timelike region follows the lines of previous works for the  $\gamma^* N \rightarrow \Delta(1232)$  transition [14, 15] with a few modifications. We use the form,

$$G_M^\pi(q^2) = G_M^{\pi a}(0) F_\pi(q^2) \left( \frac{\Lambda_\pi^2}{\Lambda_\pi^2 - q^2} \right)^3 + G_M^{\pi b}(0) \tilde{G}_D^2(q^2), \quad (5.1)$$

where  $G_M^{\pi a}(0)$  and  $G_M^{\pi b}(0)$  are the pion contributions for the diagrams (a) and (b) at  $q^2 = 0$ , respectively,  $F_\pi(q^2)$  is the pion electromagnetic form factor,  $\Lambda_\pi^2 = 2.30 \text{ GeV}^2$ , and  $\tilde{G}_D(q^2)$  is a generalization of the traditional dipole form factor. The coefficients  $G_M^{\pi a}(0)$  and  $G_M^{\pi b}(0)$  are presented in Table II. In Eq. (5.1), we omit the dependence on  $W$ , since the coefficients  $G_M^{\pi a}(0)$  and  $G_M^{\pi b}(0)$  are determined in the physical limit ( $W = M_{B'}$ ).

The explicit form of Eq. (5.1) for  $G_M^\pi$  is motivated by the fast falloff of the pion cloud contribution in the spacelike region, which may be simulated by the  $1/Q^8$  falloff, for very large  $Q^2$  (pQCD regime). The first term includes the connection to the pion form factor  $F_\pi(q^2)$  at low  $q^2$  associated with the diagram 1 (a). The second term provides a simple and effective parametrization of the contributions associated with the possible baryon intermediate states, also ruled by a falloff  $1/Q^8$ . Using pQCD arguments, one can conclude that the systems with  $n$  constituents contribute to the asymptotic form:  $G_M \propto 1/Q^{2(n-1)}$  [99, 100]. Thus, the valence quark contributions ( $n = 3$ ) are dominated by  $G_M \propto 1/Q^4$ , and contributions associated with the quark-antiquark excitations ( $n = 5$ ) are dominated by  $G_M \propto 1/Q^8$  for large  $Q^2$ .

Compared to Refs. [14, 15], we use a tripole function instead of a dipole because we replace the parametrization of  $F_\pi(q^2)$  by a function which falls off as  $F_\pi \propto 1/Q^2$ , as discussed next.

For the pion electromagnetic form factor we use a parametrization derived from VMD Lagrangian associated with the pion-rho couplings and photon-rho couplings with the form [111–117],

$$F_\pi(q^2) = \frac{m_\rho^2}{m_\rho^2 - q^2 - im_\rho \Gamma_\rho(q^2)}, \quad (5.2)$$

where  $m_\rho$  is the mass of the  $\rho$ -meson and [111, 117, 118]

$$\Gamma_\rho(q^2) = \Gamma_\rho^0 \frac{m_\rho}{\sqrt{q^2}} \left( \frac{q^2 - 4m_\pi^2}{m_\rho^2 - 4m_\pi^2} \right)^{3/2} \theta(q^2 - 4m_\pi^2), \quad (5.3)$$

where  $m_\pi$  is the pion mass,  $\theta$  is the Heaviside function and  $\Gamma_\rho^0$  is a constant associated with the  $\rho \rightarrow \pi\pi$  decay at the physical  $\rho$  mass ( $q^2 = m_\rho^2$ ).

In the spacelike region  $\Gamma_\rho \equiv 0$  and  $F_\pi(q^2) \propto 1/Q^2$  for large  $Q^2$ . In the timelike region, one has  $\Gamma_\rho \propto q^2$  for large  $q^2$ , consequently, we obtain  $F_\pi(q^2) \propto 1/q^2$ , for large  $q^2$ .



	$G_M^{\pi^a}(0)$	$G_M^{\pi^b}(0)$	$G_M^\pi(0)$	$G_M^{K^a}(0)$	$G_M^{K^b}(0)$	$G_M^K(0)$	$G_M^B(0, M_{B'})$	$\alpha_\pi(\%)$	$\alpha_K(\%)$
$\gamma^* N \rightarrow \Delta$	0.713	0.610	1.323	0.0167	0.0367	0.0534	1.633	44.0	1.8
$\gamma^* \Lambda \rightarrow \Sigma^{*0}$	0.669	0.358	1.027	0.0670	0.2768	0.3438	1.683	36.0	11.3
$\gamma^* \Sigma^+ \rightarrow \Sigma^{*+}$	0.149	0.513	0.663	0.1527	0.2640	0.4167	2.094	20.9	13.1
$\gamma^* \Sigma^0 \rightarrow \Sigma^{*0}$	0.000	0.270	0.270	0.1019	0.1001	0.2020	0.969	18.7	14.0
$\gamma^* \Sigma^- \rightarrow \Sigma^{*-}$	-0.149	0.026	-0.124	0.0510	-0.0638	-0.0128	-0.156	42.3	4.4
$\gamma^* \Xi^0 \rightarrow \Xi^{*0}$	0.222	0.086	0.308	0.1850	0.5126	0.6976	2.191	9.6	21.8
$\gamma^* \Xi^- \rightarrow \Xi^{*-}$	-0.222	0.084	-0.138	0.0370	-0.1070	-0.0700	-0.168	36.7	18.6

TABLE II. Coefficients of the meson cloud contributions. The column with  $G_M^B(0, M_{B'})$  include the bare contribution at  $q^2 = 0$ . The last two columns indicate the fraction of pion and kaon cloud for  $G_M(0, M_{B'})$ .

In the expressions (5.2) and (5.3),  $m_\rho$  ( $\rho$ -meson dressed mass) and  $\Gamma_\rho^0$  can be calculated using a parametrization of the  $|F_\pi(q^2)|^2$  data. The physical value of  $m_\rho$  is not very precise because one obtains different estimates depending on the experiment ( $\rho^0 \rightarrow \pi^+\pi^-$  decay,  $\rho^\pm$  decays, hadronic production etc.) [21, 119]. In the literature, it was also discussed that the data associated with  $|F_\pi(q^2)|^2$  cannot be described accurately by the relativistic Breit-Wigner from Eq. (5.3) and it requires some additional shape parameters [117, 119, 120]. It is also worth noticing that near the peak ( $q^2 \simeq m_\rho^2 \simeq 0.6 \text{ GeV}^2$ ) the function  $|F_\pi(q^2)|^2$  has contributions associated with the  $\omega \rightarrow \pi\pi$  decay (isoscalar contribution) due to the  $\rho$ - $\omega$  mixing. Since our purpose is to parametrize the isovector contributions, we ignore those effects and determine the values of  $m_\rho$  and  $\Gamma_\rho^0$  by a fit to the  $|F_\pi(q^2)|^2$  in the range  $-1 \text{ GeV}^2 < q^2 < 1 \text{ GeV}^2$ . For larger values of  $q^2$  there are contamination of poles associated with higher mass excitations of the  $\rho$ . From the fit, we obtain the values

$$m_\rho = 0.771 \text{ GeV}, \quad \Gamma_\rho^0 = 0.117 \text{ GeV}. \quad (5.4)$$

The results of the fit are presented in Appendix B.

The parametrization of  $|F_\pi(q^2)|$  by Eqs. (5.2) and (5.3) is important because it includes the analytic structure associated with the two-pion cut in an exact form. In addition, we ensure that we have the correct falloff for  $F_\pi(q^2)$  for large  $Q^2 = -q^2$ . More details about the calibration based on Eq. (5.1) are included in Appendix B.

We discuss now the function  $\tilde{G}_D$ . Following Ref. [14], the function  $\tilde{G}_D$  is defined by

$$\tilde{G}_D(q^2) = \frac{\Lambda_D^4}{(\Lambda_D^2 - q^2)^2 + \Lambda_D^2 \Gamma_D^2}, \quad (5.5)$$

where  $\Lambda_D^2 = 0.9 \text{ GeV}^2$  and  $\Gamma_D(q^2)$  is an effective width. For  $\Gamma_D(q^2)$ , we use parametrization [14, 25, 27]

$$\Gamma_D(q^2) = 4\Gamma_D^0 \left( \frac{q^2}{\Lambda_D^2 + q^2} \right)^2 \theta(q^2), \quad (5.6)$$

where  $\theta$  is the Heaviside function and  $\Gamma_D^0 = 4\Gamma_\rho^{\text{exp}}$ . Here  $\Gamma_\rho^{\text{exp}} \simeq 0.149 \text{ GeV}$  is the experimental value of the  $\rho$  decay width. The form (5.6) provides a smooth continuous

transition between the spacelike and the timelike region.<sup>2</sup> The function  $\Gamma_D(q^2)$  converge to  $\Gamma_D^0$  for very large  $q^2$  and spread out the effect of the pole  $q^2 = \Lambda_D^2$  [14, 15].

## B. Kaon cloud contributions

The extension of the kaon cloud contribution to the timelike region follows lines similar to the pion cloud contribution of Eq. (5.1). We use then

$$G_M^K(q^2) = G_M^{K^a}(0) F_K(q^2) \left( \frac{\Lambda_{K^a}^2}{\Lambda_{K^a}^2 - q^2} \right)^3 + G_M^{K^b}(0) \tilde{G}_{DK}^2(q^2), \quad (5.7)$$

where  $G_M^{K^a}(0)$  and  $G_M^{K^b}(0)$  are the kaon contributions for the diagrams (a) and (b), respectively,  $F_K$  is the kaon electromagnetic form factor,  $\Lambda_{K^a}$  is a new cutoff, and  $\tilde{G}_{DK}$  is a new dipole form factor.

For the kaon form factor, we use

$$F_K(q^2) = \frac{\Lambda_K^2}{\Lambda_K^2 - q^2}, \quad (5.8)$$

where  $\Lambda_K^2$  is determined by the kaon square radius  $r_K^2 = 0.314 \pm 0.035 \text{ fm}^2$  [21]. One obtains then  $\Lambda_K^2 \simeq 0.745 \text{ GeV}^2$ . The monopole form (5.8) of  $F_K$  is motivated by pQCD according to the expected falloff  $F_K \propto 1/q^2$  for a  $q\bar{q}$  system [99, 100]. The inclusion of the tripole factor is also motivated by pQCD arguments. One expects that the falloff of the baryon-meson system to be  $1/q^8$  due to the number of constituents (three quarks plus a quark-antiquark pair) [100].

As for  $\tilde{G}_{DK}$ , one considers a form similar to Eq. (5.5),

$$\tilde{G}_{DK}(q^2) = \frac{\Lambda_{K^b}^4}{(\Lambda_{K^b}^2 - q^2)^2 + \Lambda_{K^b}^2 \Gamma_{K^b}^2}, \quad (5.9)$$

<sup>2</sup> Thus, although the regularization generates spurious imaginary contributions below the physical thresholds ( $4m_\pi^2, 9m_\pi^2$  related to vector meson poles), those contributions are small at low  $q^2$  (proportional to  $q^4$ ) and interfere minimally with the imaginary contributions associated with the physical poles.

	$\frac{d \log G_M^{Ka}}{dq^2}(0)$	$\Lambda_{Ka}^2$	$\frac{d \log G_M^{Kb}}{dq^2}(0)$	$\Lambda_{Kb}^2$
$\gamma^* N \rightarrow \Delta$	-2.89	1.944	-2.05	1.951
$\gamma^* \Lambda \rightarrow \Sigma^{*0}$	-3.20	1.618	-5.40	0.741
$\gamma^* \Sigma^+ \rightarrow \Sigma^{*+}$	-2.93	1.889	-2.37	1.688
$\gamma^* \Sigma^0 \rightarrow \Sigma^{*0}$	-2.99	1.825	-2.43	1.645
$\gamma^* \Sigma^- \rightarrow \Sigma^{*-}$	-3.15	1.660	-2.17	1.841
$\gamma^* \Xi^0 \rightarrow \Xi^{*0}$	-2.98	1.829	-3.37	1.186
$\gamma^* \Xi^- \rightarrow \Xi^{*-}$	-2.84	2.000	-2.33	1.715

TABLE III. Logarithmic derivatives of the kaon cloud contributions and cutoffs  $\Lambda_{Ka}$  and  $\Lambda_{Kb}$ . The derivatives are in units  $\text{GeV}^{-2}$ . The square cutoffs are in units  $\text{GeV}^2$ . Details of the calculations are presented in Appendix C.

where  $\Lambda_{Kb}$  is a new cutoff, and  $\Gamma_{Kb}$  is an effective decay width defined by Eq. (5.6) with  $\Gamma_D \leftrightarrow \Gamma_{Kb}$  and  $\Lambda_D \rightarrow \Lambda_{Kb}$ . Also here, the falloff is  $1/q^8$ .

To calculate the kaon cloud contribution, one needs to know the coefficients  $G_M^{Ka}(0)$  and  $G_M^{Kb}(0)$  and the cutoffs  $\Lambda_{Ka}$  and  $\Lambda_{Kb}$ , which depend on the decuplet and octet baryon states. The coefficients  $G_M^{Ka}(0)$  and  $G_M^{Kb}(0)$  were determined by the previous work about the decuplet baryon radiative decays [37] and are presented in Table II. The determination of the cutoffs  $\Lambda_{Ka}$  and  $\Lambda_{Kb}$  require a microscopic calculation of the kaon cloud contribution for non-zero values of  $q^2$ . The method used to calculate  $\Lambda_{Ka}$  and  $\Lambda_{Kb}$ , is explained in the next section. Recall that in the case of the pion cloud, the free parameters from (5.1), are determined directly from the comparison with the physical data [14, 71].

In the case of the cutoffs  $\Lambda_{Ka}$  or  $\Lambda_{Kb}$ , when they have a magnitude close to  $(M_{B'} - M_B)$ , one needs to regularize the contributions of those poles to the transition form factors, including an effective width, as in the case of Eq. (5.6).

In the last three columns of Table II, we include for convenience of the discussion: the bare contribution  $G_M^B(0, M_{B'})$  to the magnetic form factor at  $q^2 = 0$ , and the relative contributions of the pion ( $\alpha_\pi$ ) and kaon ( $\alpha_K$ ) to the final results also at  $q^2 = 0$ . These contributions are estimated by  $G_M^m(0)/[G_M^\pi(0) + G_M^K(0) + G_M^B(0, M_{B'})]$ , where  $m = \pi, K$ .

### 1. Determination of the kaon cloud cutoffs

The calculation of the kaon cloud contributions for finite  $q^2$  requires an extension of the calculations for the case  $q^2 = 0$  from Ref. [37] for the case  $q^2 \neq 0$ . For the present discussion, it is not important if  $q^2 > 0$  or  $q^2 < 0$ . One can then consider the case  $Q^2 = -q^2 > 0$ . For simplicity, we use  $G_M^{K\ell}(Q^2)$  to represent  $G_M^{K\ell}(q^2)$ .

We examine then the calculation of the diagrams from Fig. 1,  $G_M^{K\ell}(Q^2)$ , where  $\ell = a, b$ , for positive values of  $Q^2$  near  $Q^2 = 0$ . In the present work, we are interested in small values of  $Q^2$ , since the range of the cal-

culations is restricted to  $-(M_{B'} - M_B)^2 \leq Q^2 \leq 0$  and  $(M_{B'} - M_B)^2 \leq 0.1 \text{ GeV}^2$  in most cases.

In the CBM the calculation of  $G_M^{K\ell}(Q^2)$  must be performed in a specific frame. We choose then the Breit frame, because it is more accurate due to the kinematic approximations used in the calculations at  $Q^2 = 0$ , more specifically the static approximation (or the heavy baryon approximation). In the static approximation,

$$Q^2 = Q_{st}^2 \simeq \mathbf{q}^2 - (M_{B'} - M_B)^2, \quad (5.10)$$

where the label "st" stands for *static approximation*. The relative error in the approximation for  $q_0 \simeq (M_{B'} - M_B)$  is of the order of  $-\frac{1}{8M_B^2}(M_{B'} - M_B)^2 - \frac{1}{16M_B^2}Q^2$ . A small error<sup>3</sup> for small values of  $Q^2$ .

In these conditions, we can use the expansion,

$$G_M^{K\ell}(Q^2) = G_M^{K\ell}(0) + \left[ \frac{dG_M^{K\ell}}{dq^2}(0) \right] Q^2. \quad (5.11)$$

From the above relation, we can conclude that the first finite correction to  $G_M^{K\ell}(0)$  can be determined by the coefficient of the expansion in  $Q^2 = \mathbf{q}^2 - q_0^2$ , which can be determined by the derivative on  $\mathbf{q}^2$  for  $\mathbf{q}^2 = q_0^2$ . [In the static approximation  $\frac{d}{dQ^2} \equiv \frac{d}{dQ_{st}^2} \equiv \frac{d}{d\mathbf{q}^2}$ ].

The consequence of this discussion is that, to estimate the cutoffs associated with (5.7), we do not need to calculate  $G_M^{K\ell}(Q^2)$  for a specific value for  $Q^2$ . It is sufficient, instead, to calculate the derivative  $\frac{d}{d\mathbf{q}^2}G_M^{K\ell}(Q_{st}^2 = 0)$ . The numerical values for  $G_M^{K\ell}(0)$  are already presented in Table II. The expressions for  $G_M^{K\ell}(0)$  and  $\frac{dG_M^{K\ell}}{dq^2}(0)$  are presented in Appendix D.

For the following discussion, it is convenient to normalize Eq. (5.11) by the value of  $G_M^{K\ell}(0)$ ,

$$\frac{G_M^{K\ell}(Q^2)}{G_M^{K\ell}(0)} = 1 + \left[ \frac{d \log G_M^{K\ell}}{dq^2}(0) \right] Q^2. \quad (5.12)$$

<sup>3</sup> In the baryon  $B'$  rest frame the relative error is  $\frac{Q^2}{M_{B'}^2 - M_B^2}$ .

Notice that  $\frac{1}{F(0)} \frac{dF}{dQ^2}(0) \equiv \frac{d \log F}{dQ^2}(0)$  for a generic function  $F(Q^2)$ . One concludes, then, that what we need for our calculations is in fact the logarithmic derivative.

The numerical values of the logarithmic derivatives of  $G_M^{K\ell}$  at  $Q^2 = 0$  are presented in Table III. The value of  $G_M^{K\ell}(0)$  is the same as in Table II and in previous works, where the meson cloud contributions from the CBM are calibrated by pion cloud contributions to the  $\gamma^* N \rightarrow \Delta$  transitions. In Appendix D, this procedure is explained in detail.

To determine the unknown cutoffs from (5.7), one considers low- $Q^2$  expansions of the multipoles associated with the diagrams (a) and (b) from Fig. 1.

For the diagram (a), we use

$$\begin{aligned} F_K(q^2) \left( \frac{\Lambda_{Ka}^2}{\Lambda_{Ka}^2 - q^2} \right)^3 &\simeq \left( 1 - \frac{Q^2}{\Lambda_K^2} \right) \left( 1 - 3 \frac{Q^2}{\Lambda_{Ka}^2} \right) \\ &\simeq 1 - \left( \frac{1}{\Lambda_K^2} + \frac{3}{\Lambda_{Ka}^2} \right) Q^2, \end{aligned} \quad (5.13)$$

drooping terms of the order  $Q^4$ . From the comparison between Eqs. (5.12) and (5.13), one concludes that

$$\frac{1}{\Lambda_K^2} + \frac{3}{\Lambda_{Ka}^2} \simeq - \frac{d \log G_M^{Ka}}{dQ^2}(0). \quad (5.14)$$

This relation can be used to calculate  $\Lambda_{Ka}^2$  based on the value of  $\Lambda_K^2$  extracted from the experimental value for  $r_K^2$ , and the values of the logarithm derivatives from Table III.

As for the diagram (b), one obtains in the regime  $Q^2 > 0$ ,

$$\begin{aligned} \tilde{G}_{DK}(q^2) &= \left( \frac{\Lambda_{Kb}^2}{\Lambda_{Kb}^2 + Q^2} \right)^4 \\ &\simeq 1 - 4 \frac{Q^2}{\Lambda_{Kb}^2}. \end{aligned} \quad (5.15)$$

From the comparison with (5.12), we conclude that

$$\frac{4}{\Lambda_{Kb}^2} = - \frac{d \log G_M^{Kb}}{dQ^2}(0), \quad (5.16)$$

which can be used to calculate  $\Lambda_{Kb}^2$  based on the values of the logarithm derivatives from Table III.

## 2. Discussion about the kaon cloud contributions

The kaon cloud contribution to the  $B' \rightarrow \gamma^* B$  transition can now be determined using Eq. (5.7), the coefficients  $G_M^{Ka}(0)$  and  $G_M^{Kb}(0)$  from Table II, and the square cutoffs  $\Lambda_{Ka}^2$  and  $\Lambda_{Kb}^2$  from Table III.

The values presented in Table II are based on the calculations from Ref. [37]. In the case of the values associated with the kaon cloud, there are minor differences

compared with the previous calculation. That happens, because we recalculate  $G_M^{K\ell}(0)$  using a more precise numerical integration algorithm, and because we present the results with more digits. This is justified since the focus is on the kaon cloud and it is necessary to include more precision of the calculations. In the limit  $q^2 = 0$ , the results are qualitatively equivalent to the results from Ref. [37]. The differences between the calculations from Ref. [37] are apparent, namely, only in the third digit of the final results.

A comment about the results for the  $\gamma^* \Sigma^0 \rightarrow \Sigma^{*0}$  is in order. In the Table III from Ref. [37], there was a typo in the value of  $G_M^{Kb}(0)$  (0.010), which is corrected in the present work to 0.1001 in Table II. The typo, however, did not affect the final results. In the present work, we conclude that the contribution of the kaon cloud to the transition form factor is in fact 0.2020.

We can use the results  $G_M^\pi(0)$  and  $G_M^K(0)$  from Table II to discuss the magnitude of the pion and kaon cloud contributions to the transition form factors at the photon point according to the relative contributions of the pion ( $\alpha_\pi$ ) and the kaon ( $\alpha_K$ ) displayed in the last two columns (in a percentage). In a first analysis, we exclude the  $\gamma^* \Sigma^- \rightarrow \Sigma^{*-}$  and  $\gamma^* \Xi^- \rightarrow \Xi^{*-}$  transitions because the contributions of the valence quarks are very small as discussed in Sec. III [a consequence of  $U$ -spin and  $SU(3)$  symmetries].

From the results from Table II, we can conclude that the pion cloud is very important for the  $\gamma^* N \rightarrow \Delta$ ,  $\gamma^* \Lambda \rightarrow \Sigma^{*0}$  and  $\gamma^* \Sigma \rightarrow \Sigma^*$  transitions, with contributions of about 44%, 36% and 20%, in that order. As for the kaon cloud, it is important for the  $\gamma^* \Lambda \rightarrow \Sigma^{*0}$  and  $\gamma^* \Sigma \rightarrow \Sigma^*$  transitions (10-15%), and much more relevant for the  $\gamma^* \Xi^0 \rightarrow \Xi^{*0}$  transition (22%). These results support the need of incorporating the kaon cloud contributions in the calculations of transition form factors.

Concerning the  $\gamma^* \Sigma^- \rightarrow \Sigma^{*-}$  and  $\gamma^* \Xi^- \rightarrow \Xi^{*-}$  transitions, the meson cloud (pion or kaon) effects have an important relative contribution, close to 50%, because their magnitudes are comparable with the valence quark contributions.

## VI. RESULTS FOR THE TRANSITION FORM FACTORS

In this section we present our results for the transition form factors between octet baryons and decuplet baryons.

For the numerical calculation, we use the experimental octet baryon mass values:  $M_N = 0.939$  GeV,  $M_\Lambda = 1.116$  GeV,  $M_\Sigma = 1.192$  GeV, and  $M_\Xi = 1.318$  GeV. As before,  $W$  represents the decuplet baryon masses. In the calculations associated with the physical decuplet baryons, we use the physical masses:  $M_\Delta = 1.232$  GeV,  $M_{\Sigma^*} = 1.385$  GeV and  $M_{\Xi^*} = 1.533$  GeV.

The results are presented in Fig. 2 for different values of  $W$  close to the physical pole mass value  $M_{B'}$ . The final results (bare plus meson cloud) are represented by

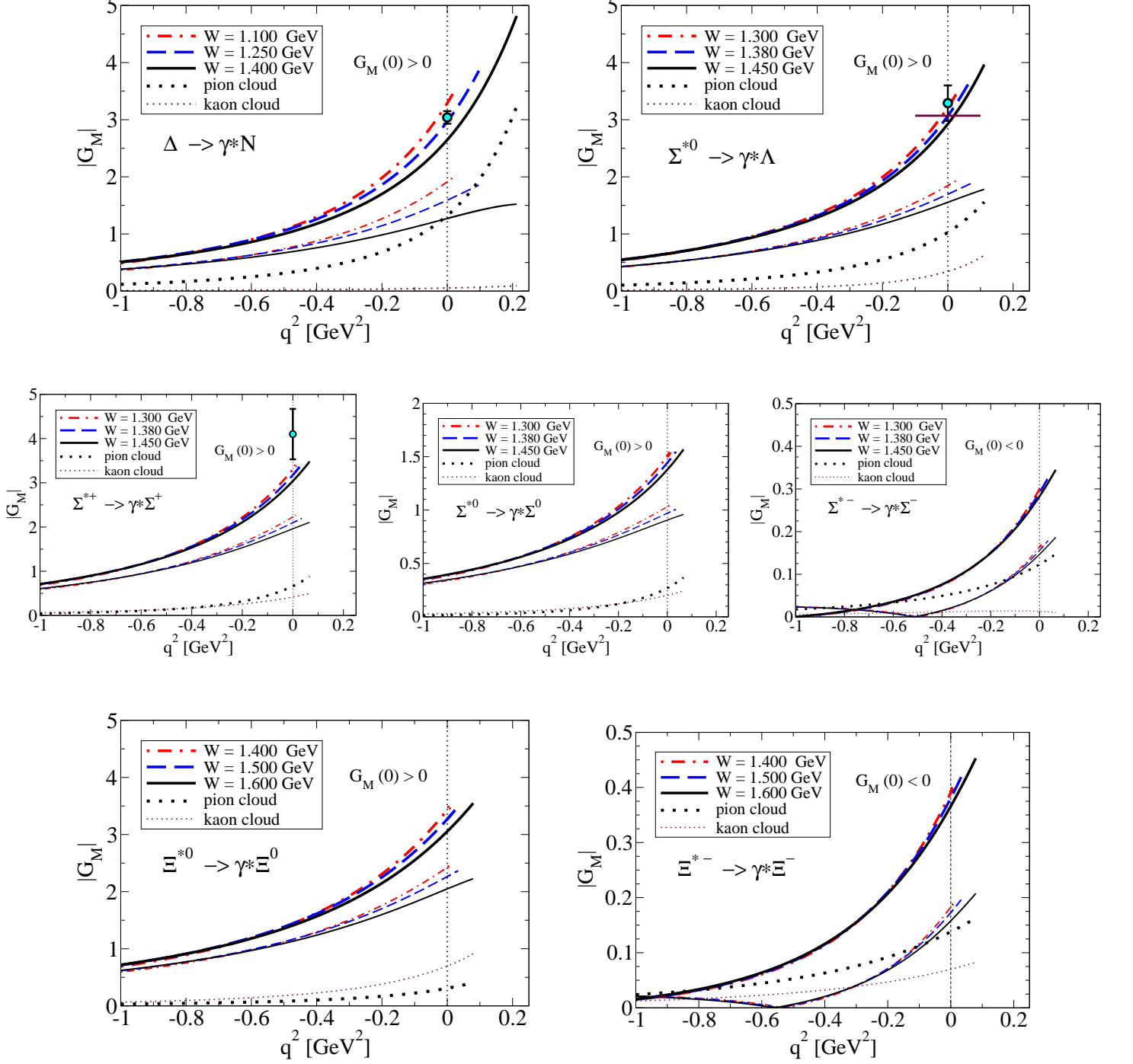


FIG. 2. Magnitude of transition form factor  $G_M$ . The thick lines represent the total (valence plus pion and kaon clouds) and the thin lines represent the valence quark contribution. The thick dotted line and the thin dotted represent the pion and kaon cloud contributions, respectively. The Data are from Table IV.

the thick lines. The bare contributions are represented by the corresponding thinner lines. In the graphs, we include also the contributions of the pion and kaon clouds associated with the maximum value of  $W$  (dotted lines). The pion and kaon cloud contributions for the first and second values of  $W$  are described by the same line, except

that they are limited to  $q^2 \leq (W - M_B)^2$ . Recall that our parametrization of the meson cloud contributions is independent of  $W$ .

In Fig. 2, one can see the significant contributions from the kaon cloud in all the transitions, except for the  $\Delta \rightarrow \gamma^* N$  and  $\Sigma^{*-} \rightarrow \gamma^* \Sigma^-$  transitions. In the first case

	$G_M(0) _{\text{no}K}$	$G_M(0) _K$	$G_M(0)$	$ G_M(0) _{\text{exp}}$	$\Gamma_{\gamma B}(\text{keV})$	$\Gamma_{\gamma B}^{\text{exp}}(\text{keV})$
$\Delta \rightarrow \gamma N$	2.96	0.053	3.01	$3.04 \pm 0.11$ [121]	644	$660 \pm 47$ [121]
$\Sigma^{*0} \rightarrow \gamma \Lambda$	2.71	0.344	3.05	$3.35 \pm 0.57$ [121] $3.26 \pm 0.37$ [64]	392	$470 \pm 160$ [121] $445 \pm 102$ [64]
$\Sigma^{*+} \rightarrow \gamma \Sigma^+$	2.76	0.417	3.17	$4.10 \pm 0.57$ [122]	149	$250 \pm 70$ [122]
$\Sigma^{*0} \rightarrow \gamma \Sigma^0$	1.24	0.202	1.44	$< 11$ [123]	31	$< 1750$ [123]
$\Sigma^{*-} \rightarrow \gamma \Sigma^-$	-0.280	-0.013	-0.291	$< 0.8$ [124]	1.3	$< 9.5$ [124]
$\Xi^{*0} \rightarrow \gamma \Xi^0$	2.50	0.698	3.20		172	
$\Xi^{*-} \rightarrow \gamma \Xi^-$	-0.306	-0.070	-0.376	$< 4.2$ [125]	2.4	$< 366$ [125]

TABLE IV. Results for  $G_M(0)$  corresponding to the  $B' \rightarrow \gamma B$  decays.  $G_M(0)|_{\text{no}K}$  gives the result without the kaon cloud (bare plus pion cloud).  $G_M(0)|_K$  represents exclusively the kaon cloud contribution (no bare core term). The values for  $|G_M(0)|_{\text{exp}}$  are estimated using the experimental values of  $\Gamma_{\gamma B}$  ( $\Gamma_{\gamma B}^{\text{exp}}$ ). The  $\eta$  cloud contributions are in general negligible—the exception is the  $\Xi^{*0} \rightarrow \gamma \Xi^0$  transition (0.086) [37]. For the  $\Sigma^{*0} \rightarrow \gamma \Lambda$ , we consider the average  $|G_M(0)| = 3.29 \pm 0.31$  and  $\Gamma_{\gamma B} = 452 \pm 86$  keV.

the kaon cloud effects are in fact very small (from both diagrams). In the second case, there is a strong cancellation between the contributions from the diagrams (a) and (b), as can be confirmed by the values of the coefficients  $G_M^{Ka}(0)$  and  $G_M^{Kb}(0)$  in Table II.

The enhancement of  $|G_M|$  by the kaon cloud in the timelike region is more pronounced for the  $\Sigma^{*0} \rightarrow \gamma^* \Lambda$  and  $\Xi^{*0} \rightarrow \gamma^* \Xi^0$  transitions. In the first case the reason is due to the small magnitude of the cutoff  $\Lambda_{Kb}$  [sharper contribution from the diagram (b) near  $Q^2 = 0$ ]. In the second case, the kaon cloud coefficients are large (see Table II).

We do not make a detailed comparison of our calculations with those in the literature, because the comparison was already presented in previous works for the case  $q^2 = 0$  [37] and for  $q^2 > 0$  with the meson cloud restricted to the pion cloud (see Sec. III E in Ref. [15]). One can, nevertheless, compare our bare estimates with other calculations of transition form factors for finite  $q^2$  based on quark degrees of freedom as in Refs. [57, 63].

The calculations from Ref. [57] are based on the Dyson-Schwinger framework. Their results are similar to our estimates for  $G_M^B$  for  $q^2 < -1$  GeV<sup>2</sup>. There are also calculations based on an  $SU(3)$  chiral quark-soliton model [63], which include some pion cloud effects. The estimates of the contribution of the bare core for  $q^2 = 0$  are similar to our estimates. The results for  $G_M$  including meson cloud, however, have slower falloffs with  $Q^2 = -q^2$ , when compared to our estimates.

## VII. RESULTS FOR THE RADIATIVE AND DALITZ DECAY WIDTHS

In this section, we discuss our results for the radiative and the Dalitz decay widths associated with the baryon decuplet  $B'$  decays to baryon octet  $B$ .

### A. Radiative decays

Our results for the radiative decay widths are a consequence of our estimate for  $|G_M(0)|$  based on the dominance of magnetic dipole form factor.

The comparison between our estimates for  $|G_M(0)|$  and  $\Gamma_{\gamma B}(M_{B'})$  are presented in Table IV. The experimental values for  $|G_M(0)|$  are determined by Eq. (2.9), except for the  $\Delta(1232) \rightarrow \gamma N$  decay, where  $G_M(0)$  is measured explicitly [21]. Notice that there are data only for the  $\Delta \rightarrow \gamma N$ ,  $\Sigma^{*0} \rightarrow \gamma \Lambda$  and  $\Sigma^{*+} \rightarrow \gamma \Sigma^+$  decays. In the case of the  $\Sigma^{*0} \rightarrow \gamma \Sigma^0$ ,  $\Sigma^{*-} \rightarrow \gamma \Sigma^-$  and  $\Xi^{*-} \rightarrow \gamma \Xi^-$  decays, we present also the experimental limits (lower limit of the detectors).

In Table IV, we display also our estimate without the inclusion of the kaon cloud,  $G_M(0)|_{\text{no}K}$ , and the contribution of the kaon cloud,  $G_M(0)|_K$ . The enhancement of  $\Gamma_{\gamma B}$  due to the kaon cloud can be inferred from the comparison of the two columns. One can then conclude that the kaon cloud contributions increase the radiative decays of the  $\Sigma^*$  in about 25–30%, except for the  $\Sigma^{*0}$ , and in about 50% for the  $\Xi^*$  decays.

Concerning the cases for which there are no measurements of the Dalitz decay widths, we have a few remarks.

There is the expectation that, with the increasing of strangeness production in facilities such as HADES and PANDA [19, 30–32], that the  $\Xi^{*0} \rightarrow \gamma \Xi^0$  and  $\Sigma^{*0} \rightarrow \gamma \Sigma^0$  decay widths may be measured, since their magnitudes are comparable to the  $\Sigma^{*+} \rightarrow \gamma \Sigma^+$  decay width. The estimated  $\Sigma^{*0} \rightarrow \gamma \Sigma^0$  decay width is smaller than the previous three cases, but we recall that  $SU(3)$  and  $U$ -spin symmetry based calculations (see Sec. IV D), suggest that its magnitude is about one fourth of the  $\Sigma^{*+} \rightarrow \gamma \Sigma^+$  decay width, a reduction of less than an order of magnitude.

As for the  $\Sigma^{*-} \rightarrow \gamma \Sigma^-$  decay, for which we may expect a very small value [zero in the exact  $SU(3)$  symmetry limit]. One notices, however, that our model estimate,  $|G_M(0)| \simeq 0.3$ , is very close to the experimental

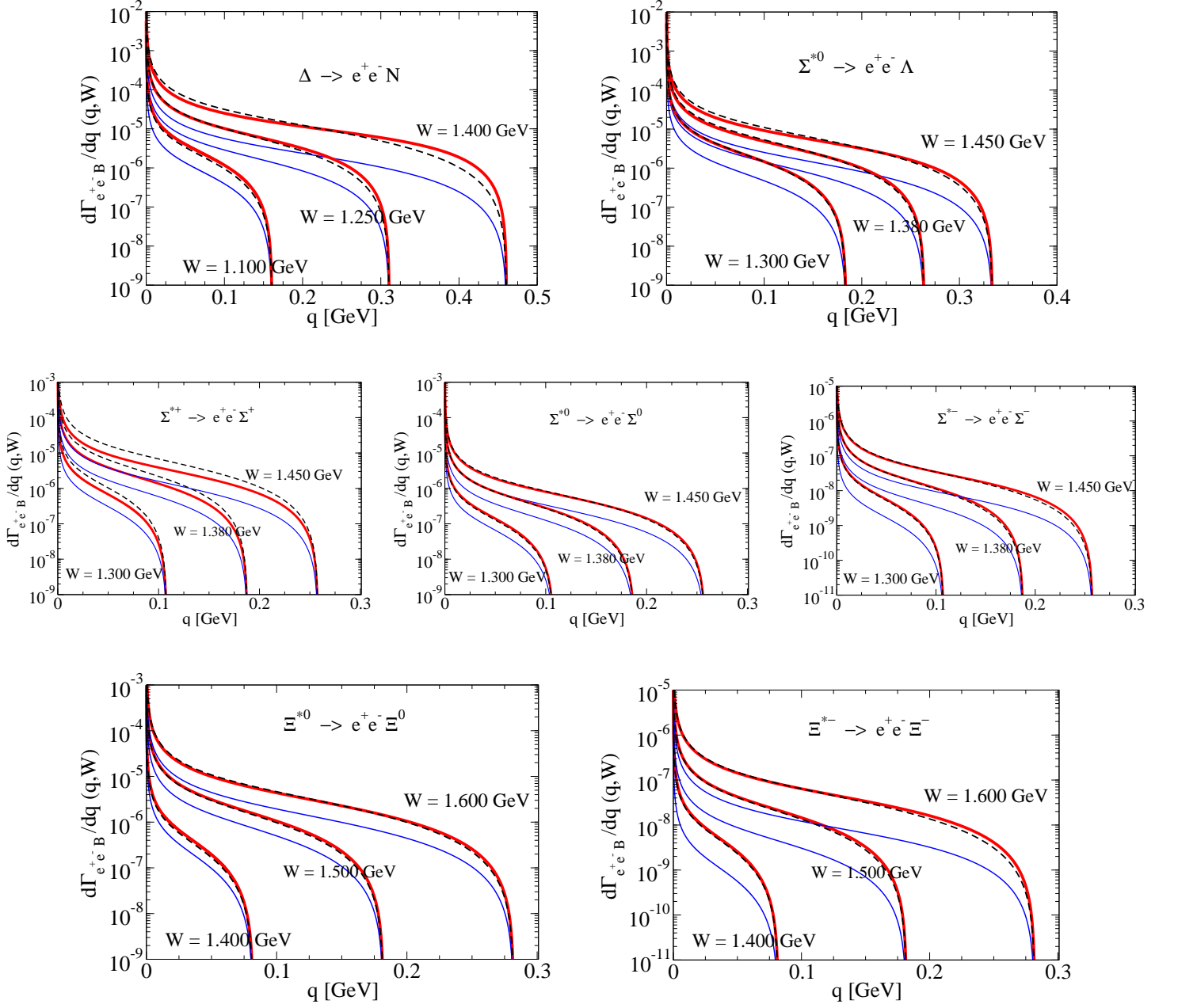


FIG. 3. Dalitz decay rates  $\frac{d}{dq}\Gamma_{e^+e^-B}$  for different values of  $W$ . Note the differences in the scales. The thick solid lines represent our final result (bare plus meson cloud). The thin solid lines represent the bare quark approximations. The results of the constant form factor model ( $G_M(q^2, W) \rightarrow G_M(0, W)$ ) are indicated by the dashed lines.

limit ( $< 0.8$ ). Finally, we point out that the estimated  $\Xi^{*-} \rightarrow \gamma \Xi^-$  decay width has a magnitude close to the  $\Sigma^{*-} \rightarrow \gamma \Sigma^-$  decay width. A small improvement of the experimental precision may be sufficient to measure the  $\Sigma^{*-}$  and  $\Xi^{*-}$  radiative decays.

## B. Dalitz decay rates

The derivatives of the Dalitz decay ( $B' \rightarrow e^+e^-B$ ) width (Dalitz decay rates) for the possible decays of decuplet baryons to octet baryons are presented in Fig. 3, for several values of  $W$ , near the decuplet baryon pole mass.

Notice that, although we use the sub-index  $e^+e^-B$ , these functions can be used for the  $B' \rightarrow \mu^+\mu^-B$  decay rates if we replace the range  $2m_e \leq q \leq (W - M_B)$

by  $2\mu \leq q \leq (W - M_B)$ , where  $2m_e \simeq 10^{-3}$  GeV and  $2\mu \simeq 0.2$  GeV.

In Fig. 3, we represent the full result (bare plus meson cloud) by the thick lines and the result of the bare contribution by the thin lines. It is clear from the graphs that, if we exclude the meson cloud contributions (thin lines, bare contributions) we underestimate the final results by about 1 order of magnitude.

For the discussion about the impact of including the  $q^2$  dependence of the form factors on the Dalitz decay processes, we include also the estimates of the Dalitz decay rates based on the QED approximation (which neglects the  $q^2$  dependence on  $G_M$ ), when we replace  $|G_M(q^2, W)|$  by  $|G_M(0, M_{B'})|$  (value of  $G_M$  at the pole). We refer to this result also as the constant form factor model. This result is represented by the dashed line. In the cases where  $|G_M(0, M_{B'})|$  are known,  $\Delta \rightarrow e^+e^-N$ ,  $\Sigma^{*0} \rightarrow e^+e^-\Lambda$ , and  $\Sigma^{*+} \rightarrow e^+e^-\Sigma^+$ , we use the experimental values of  $|G_M(0, M_{B'})|$ . In the remaining cases the result of the constant form factor model is determined by our value for  $|G_M(0, M_{B'})|$ .

Notice that, the full estimate (thick lines) and the constant form factor model (dashed lines) are very close for the  $\Sigma^{*0}$ ,  $\Sigma^{*-}$ ,  $\Xi^{*0}$  and  $\Xi^{*-}$  decays, particularly for lower values of  $q^2$ , for all values of  $W$ . From this property, we can anticipate that the results for the Dalitz di-electron decay widths from our model (with  $q^2$  dependence) and from the constant form factor model may be very close.

In the case of the  $\Sigma^{*+} \rightarrow e^+e^-\Sigma^+$ , the difference between our estimate and the constant form factor model is in part a consequence of the different estimates for  $|G_M(0, M_{\Sigma^*})|$ . Our calculation is below the experimental value in about 1.4 standard deviations (see Table IV). A similar observation is valid, but with a smaller impact for the  $\Sigma^{*0} \rightarrow e^+e^-\Lambda$  decay.

In the case of the  $\Delta \rightarrow e^+e^-N$ , and  $\Sigma^{*0} \rightarrow e^+e^-\Lambda$  decays, one can notice a deviation from the constant form factor model when  $W$  increases. This effect is a consequence of the dependence of  $|G_M|$  on  $W$ , since the  $W$  dependence is absent in the constant form factor model.

### C. Dalitz decay widths

The results of the integration of the Dalitz decay rates in  $q$ , in terms of  $W$ , the Dalitz decay widths, are presented in Fig. 4. We use dashed lines to represent  $\Gamma_{e^+e^-B}(W)$ . The thick lines represent our model and the thin lines represent the constant form factor model. The bands in the graphs for  $\Gamma_{e^+e^-B}(W)$  indicate the result at the pole ( $W = M_{B'}$ ). In the cases the value of  $G_M(0, M_{B'})$  are known, we include the window of variation associated with the estimate associated with the constant form factor model.

For the first three decays ( $\Delta \rightarrow e^+e^-N$ ,  $\Sigma^{*0} \rightarrow e^+e^-\Lambda$  and  $\Sigma^{*+} \rightarrow e^+e^-\Sigma^+$ ), we can notice that the constant form factor model predicts larger contributions than our

model. This result is mainly a consequence of the reduction of  $|G_M(q^2, W)|$  when  $W$  increases, in our model. In the case of  $\Sigma^{*+} \rightarrow e^+e^-\Sigma^+$ , the larger difference between estimates is a consequence of our result for  $|G_M(0, W)|$ , discussed already. As for the remaining decays, we can notice that the two estimates are very close, even when  $W$  increases.

The general conclusion is that the Dalitz decay widths are sensitive to the values of  $W$  (see Fig. 4). This observation is important, because, one can obtain larger values than the results at the pole ( $\Gamma_{e^+e^-B}(M_{B'})$ ) when the measurements are performed for larger values of  $W$  ( $W > M_{B'}$ ) or smaller values when  $W$  is smaller than  $M_{B'}$ . This effect can be exemplified looking into the HADES measurements of the  $\Delta(1232)$  Dalitz decay. Those measurements were performed for  $W \simeq 1.39$  GeV, a bit above the physical mass [9]. Notice that the increasing of  $W$  implies also an increasing of the limit of the dilepton momentum  $q = W - M_N$  included in the integration.

In Fig. 4, we present also our results for the radiative decay widths in terms of  $W$  (thick solid lines). The data points close to the solid lines represent the known data for  $\Gamma_{\gamma B}(W)$  at the pole ( $W = M_{B'}$ ). The estimates from the constant form factor model are represented by the thin solid lines. In general, one can notice that the constant form factor model has larger values than our model estimate above the decuplet baryon mass pole. This happens because the value of  $|G_M(0, W)|$  is reduced when  $W$  increases (see Fig. 2). The exception is the  $\Sigma^{*+} \rightarrow e^+e^-\Sigma^+$  case, where we underestimate the QED value, because we also underestimate  $G_M$ .

### D. Dalitz di-electron decay widths at the pole

Our estimates for the Dalitz decay widths at the pole ( $W = M_{B'}$ ) are presented in Table V. For the comparison with the constant form factor model, we include also the result of the calculation  $|G_M(q^2, M_{B'})| \rightarrow |G_M(0, M_{B'})| \equiv |G_M(0)|$ , labeled as  $\tilde{\Gamma}_{e^+e^-B}$ . To determine  $|G_M(0, M_{B'})|$ , we use the procedure described in the previous sections. The estimates based on our model for  $|G_M(0, M_{B'})|$  are presented in Table IV in boldface. For discussion, we include also the  $B' \rightarrow \gamma B$  branching ratios, estimated by the data, or by our model (last four cases). In the cases in which  $|G_M(0)|$  is determined by the data, we include also the estimated error based on the quadratic relation  $\Gamma_{e^+e^-B} \propto |G_M(0)|^2$  or  $\Gamma_{e^+e^-B} \propto \Gamma_{\gamma B}$ . The errors are large (larger than 5%), because the experimental determinations of  $\Gamma_{\gamma B}$  are affected by significant errors, even when  $|G_M(0)|$  is well determined, as a consequence of the quadratic relation mentioned above.<sup>4</sup>

<sup>4</sup> The relative error in  $\Gamma_{\gamma B}$  is twice the relative error in  $|G_M(0)|$ . Thus, if  $|G_M(0)|$  is determined with a precision of 10%,  $\Gamma_{\gamma B}$  is known with a precision of 20%.

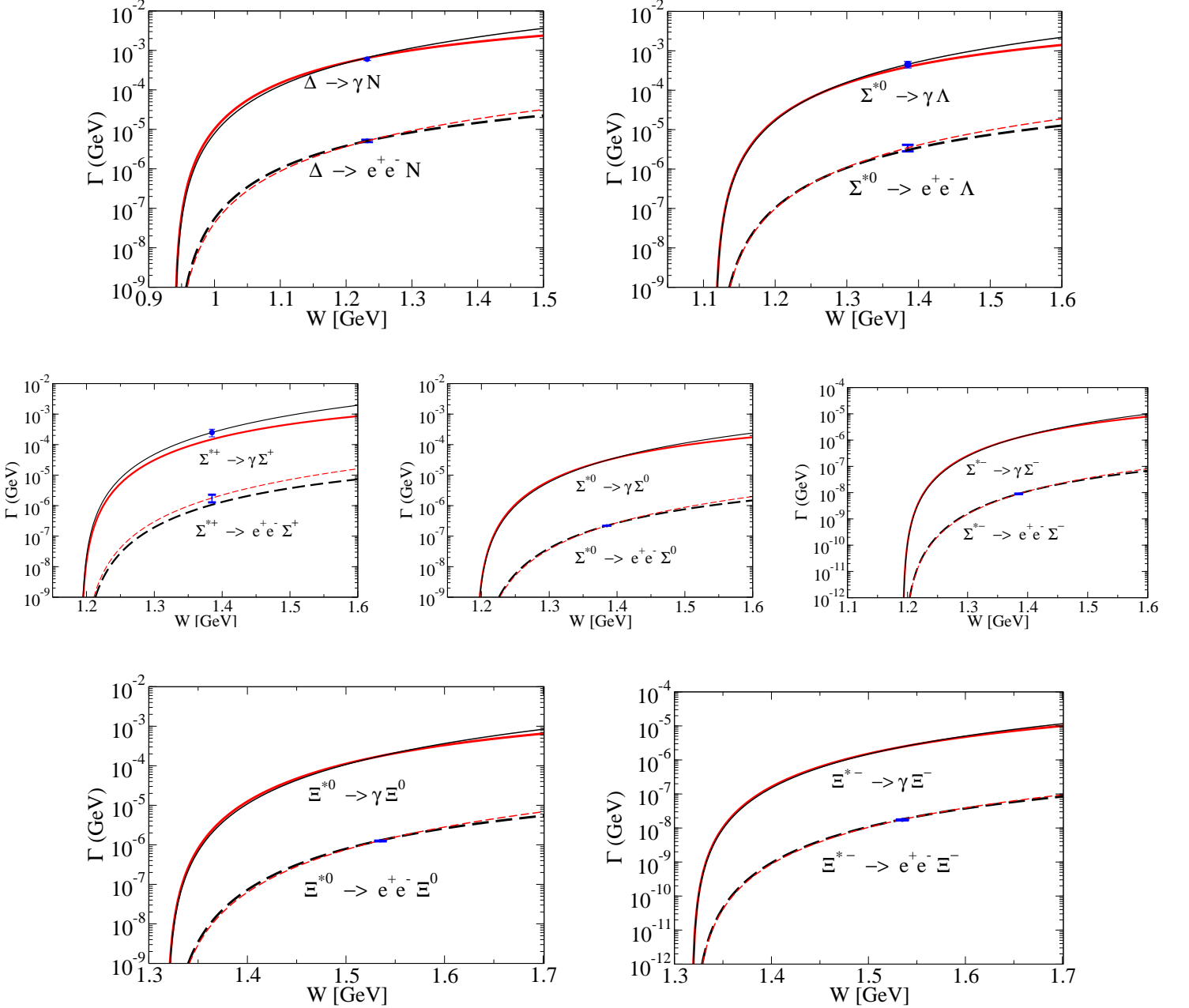


FIG. 4. Electromagnetic and Dalitz decay widths for all the decuplet decays in terms of  $W$ . The thick lines represent our model. The thin lines represent the constant form factor model. The blue bullets represent the  $\Gamma_{B' \rightarrow \gamma B}$  data from Table IV. The pair of horizontal lines represent the limits of the  $\Gamma_{B' \rightarrow e^+e^- B}$  estimate based on the constant form model, presented in Table V.

The estimates of the constant form factor model must then be taken with care due to the errors associated with  $|G_M(0)|$ . The estimate of  $\Gamma_{e^+e^- B}$  is very sensitive to the value used for  $|G_M(0)|$  or equivalently by  $\Gamma_{\gamma B}$ .

We can now discuss our estimates for the Dalitz di-electron decay widths. From the results for the last four decays ( $\Sigma^{*0,-}$  and  $\Xi^{*0,-}$ ), we conclude that there are no significant differences to the estimates based on a constant form factor. The differences between estimates are 1% at most. Since  $|G_M(0, M_{B'})|$  was also estimated by

our model, the conclusion is that the  $q^2$  dependence on the form factors is not relevant in the integration of the Dalitz di-electron decay rates. These results are expected from the results shown in Fig. 3 for the Dalitz decay rates.

Our result for the  $\Delta(1232)$  compares well with the unique measurement at HADES of the  $\Delta(1232)$  Dalitz decay at the moment. The HADES result is  $4.90 \pm 0.83$  keV [9]. The new calculation (5.10 keV), with the extra kaon cloud (4% effect) is still compatible with HADES.

When compared with our previous work [15], where the



Decay	BR( $\gamma B$ )	$\tilde{\Gamma}_{e^+e^-B}$ (keV)	$\Gamma_{e^+e^-B}$ (keV)	BR( $e^+e^-B$ )
$\Delta \rightarrow e^+e^-N$	$0.54 \times 10^{-2}$	$5.11 \pm 0.37$	5.10	$4.4 \times 10^{-5}$
$\Sigma^{*0} \rightarrow e^+e^-\Lambda$	$1.25 \times 10^{-2}$	$3.47 \pm 0.65$	3.04	$8.4 \times 10^{-5}$
$\Sigma^{*+} \rightarrow e^+e^-\Sigma^+$	$0.69 \times 10^{-2}$	$1.78 \pm 0.50$	1.07	$3.0 \times 10^{-5}$
$\Sigma^{*0} \rightarrow e^+e^-\Sigma^0$	<b><math>0.086 \times 10^{-2}</math></b>	<b>0.220</b>	0.220	$0.61 \times 10^{-5}$
$\Sigma^{*-} \rightarrow e^+e^-\Sigma^-$	<b><math>0.0036 \times 10^{-2}</math></b>	<b>0.0090</b>	0.0091	$0.023 \times 10^{-5}$
$\Xi^{*0} \rightarrow e^+e^-\Xi^0$	<b><math>1.89 \times 10^{-2}</math></b>	<b>1.253</b>	1.265	$14 \times 10^{-5}$
$\Xi^{*-} \rightarrow e^+e^-\Xi^-$	<b><math>0.023 \times 10^{-2}</math></b>	<b>0.0173</b>	0.0175	$0.18 \times 10^{-5}$

TABLE V. Decuplet baryon Dalitz di-electron decay widths using the constant form factor model ( $\tilde{\Gamma}_{e^+e^-B}$ ) and using  $G_M(q^2, M_B)$  ( $\Gamma_{e^+e^-B}$ ). The values in boldface are the estimates based on our values for  $G_M(0)$  from Table IV.

kaon cloud contributions were not taken into account, we conclude that the kaon cloud increases the Dalitz decay width in 27% for  $\Sigma^{*0} \rightarrow e^+e^-\Lambda$  decay, 30%–40% for the  $\Sigma^* \rightarrow e^+e^-\Sigma$  decays, and 50%–60% for the  $\Xi^* \rightarrow e^+e^-\Xi$  decays. The more significant enhancements in absolute values happen for  $\Sigma^{*0} \rightarrow e^+e^-\Lambda$ ,  $\Sigma^{*+} \rightarrow e^+e^-\Sigma^+$  and  $\Xi^{*0} \rightarrow e^+e^-\Xi^0$  decays. The result of  $\Xi^{*0} \rightarrow e^+e^-\Xi^0$  decay is relevant, because of its magnitude and by the expectation that the  $\Xi^*$  Dalitz decays may be measured for the first time, as a consequence of the increasing of the production of hyperons with two strange quarks at HADES [10, 19, 30, 31, 36].

Concerning the  $\Delta \rightarrow e^+e^-N$ ,  $\Sigma^{*0} \rightarrow e^+e^-\Lambda$  and  $\Sigma^{*+} \rightarrow e^+e^-\Sigma^+$  decays, our estimates are close to the estimates of the constant form factor model for the first two cases, and underestimate the result for  $\Sigma^{*+} \rightarrow e^+e^-\Sigma^+$  decay. The underestimation for the last case is a consequence of our underestimation of  $G_M$  near  $q^2 = 0$ , as explained in the previous sections. We recall that the constant form factor is determined in these cases by the experimental value for the radiative decay. The estimated errors associated with the constant form factor model are then related to the present precision for the radiative decays  $\Gamma_{\gamma B}$ .

The improvement in accuracy in the measurements of the radiative decays can help to discriminate the differences between our model and the QED estimate. If this is not possible in a near future, one should look for the results for the Dalitz decay rates,  $\frac{d}{dq}\Gamma_{e^+e^-B}(q, W)$ , as in Fig. 3, to detect differences between the two calculations.

The results for Dalitz di-electron decay rates depend on the explicit value of  $W$ , as one can conclude from the analysis of Fig. 4. It is worth noticing that given a model for  $|G_T(q^2, W)|$ , the result is closer to the constant form factor model estimate when  $W - M_B$  is small. This happens because in the calculations  $|G_T(q^2, W)|^2$  is multiplied by the factor  $(1 - q^2/(W - M_B)^2)^{3/2}$ , according to Eq. (2.1), leading to a suppression of the integrand function near  $q = W - M_B$ . Thus, the integral of the Dalitz decay rate (2.4) is dominated by  $|G_T(q^2, W)|$  near  $q^2 = 0$  when  $W - M_B$  is small, and the estimate based

on the constant form factor is a good approximation.

The results for the  $\Sigma^{*0} \rightarrow e^+e^-\Lambda$  and  $\Sigma^{*+} \rightarrow e^+e^-\Sigma^+$  decays are very important because they show that the kaon cloud contributions enhance the form factors in the timelike region, increasing the estimates which take only the pion cloud into account. This observation is particularly relevant for the diagram (b) in the  $\Sigma^{*0} \rightarrow e^+e^-\Lambda$  decay.

In a recent work, a HADES feasibility study based on the constant form factor, estimated the  $\Sigma^{*0} \rightarrow e^+e^-\Lambda$  Dalitz decay width as  $5.04 \pm 0.70$  keV [10]. This result is a consequence of the assumption of the constant form factor with  $|G_M(0)| \simeq 3.49$  (estimate based on  $\text{BR} = 1.4 \times 10^{-4}$  and  $\Gamma_{\gamma B} = 504$  keV) and an approximation in the numerical calculation (overestimate of 10%). An estimate with  $|G_M(0)| \simeq 3.49$  leads to a Dalitz decay of 3.90, about 30% below HADES feasibility estimate. The difference can also be due to different regions of  $W$  (average of the decuplet baryon mass) in the calculations.

The  $\Sigma^{*0} \rightarrow e^+e^-\Lambda$  decay widths can also be compared with estimates from chiral perturbation theory combined with dispersion relations (3.0–3.4 keV) [45].

More recently, the decuplet baryon Dalitz decays were estimated with an  $SU(3)$  symmetry breaking model [36]. The authors used a linear approximation to the transition form factors  $G(q^2) \simeq G(0) \left(1 + \frac{1}{6}q^2 \langle r \rangle^2\right)$  and calculated the interval values for the the Dalitz decay widths associated with the range  $0 \leq \langle r \rangle^2 \leq 1$  fm<sup>2</sup>. Their results are close to our results when we include the interval of variation (between 20% and 40%), except for the  $\Sigma^{*0} \rightarrow e^+e^-\Lambda$  decay width,  $2.25 \pm 0.53$  keV, a bit below our new estimate (3.04 keV).

From the analysis of the branching ratios it is interesting to notice that the largest value for the Dalitz di-electron decay is for the  $\Xi^{*0} \rightarrow e^+e^-\Xi^0$  decay, with a magnitude a bit above the  $\Sigma^{*0} \rightarrow e^+e^-\Lambda$  decay. This estimate provides an additional motivation for the experimental determination of the radiative and Dalitz di-electron decays. Another point of interest is the similarities of the magnitudes of the branching ratios for  $\Xi^{*-} \rightarrow e^+e^-\Xi^-$  and  $\Delta \rightarrow e^+e^-N$  decays, as well as

Decay	$\Gamma_{\mu^+\mu^-B}$ (eV)	$\text{BR}(\mu^+\mu^-B)$
$\Delta \rightarrow \mu^+\mu^-N$	36.3	$0.31 \times 10^{-6}$
$\Sigma^{*0} \rightarrow \mu^+\mu^-\Lambda$	9.70	$0.27 \times 10^{-6}$
$\Xi^{*0} \rightarrow \mu^+\mu^-\Xi^0$	$1.9 \times 10^{-3}$	$0.21 \times 10^{-9}$
$\Xi^{*-} \rightarrow \mu^+\mu^-\Xi^-$	$2.8 \times 10^{-5}$	$2.8 \times 10^{-12}$

TABLE VI. Decuplet baryon Dalitz di-muon decay widths and branching ratios.

$\Sigma^{*0} \rightarrow e^+e^-\Lambda$  and  $\Sigma^{*+} \rightarrow e^+e^-\Sigma^+$  decays. Notice that three of these decays are associated with channels where the radiative decay has been measured, while the  $\Xi^{*-}$  decay is strongly suppressed in the  $SU(3)$  symmetry limit [the non-zero value is a consequence of  $SU(3)$  symmetry breaking].

### E. Dalitz di-muon decay widths at the pole

Using the formalism of the Dalitz dilepton decays, we can also calculate the Dalitz decay widths into muons ( $B' \rightarrow \mu^+\mu^-B$ ), based on Eqs. (2.10)–(2.12). The results for the Dalitz di-muon decay widths and the branching ratios estimated using our values and the Particle Data Group (PDG) experimental values for the total decay widths are given in Table VI.

In the case of the di-muon decays, the  $\Sigma^* \rightarrow \Sigma$  decays are forbidden because  $2\mu > M_{B'} - M_B$  ( $\mu$  is the mass of the muon). The forbidden character of the  $\Sigma^*$  decays can be inferred from the results shown in Fig. 3 for  $W \simeq 1.38$  GeV. Notice that the upper limit  $q \simeq W - M_\Sigma \simeq 0.19$  GeV is below  $2\mu \simeq 0.21$  GeV.

The main points of interest are the magnitudes of the decay widths and branching ratios. Numerically, the  $B' \rightarrow \mu^+\mu^-B$  decay widths are better expressed in units of eV. The more relevant cases are the  $\Delta$  and  $\Sigma^{*0} \rightarrow \Lambda$  decays with branching ratios of about 2 orders of magnitude smaller than the di-electron case ( $10^{-7}$  versus  $10^{-5}$ ). Branching ratios of  $10^{-7}$  are within the accuracy of LHCb experiments [34] and are expected to be observed in BESIII and LHCb in a near future [36].

The Dalitz decay widths into di-muons for  $\Delta \rightarrow N$  and  $\Sigma^{*0} \rightarrow \Lambda$  are about 2 orders of magnitude smaller than the Dalitz decay widths into di-electrons. As for the  $\Xi^* \rightarrow \mu^+\mu^-\Xi$  decay widths, they are about  $10^{-6}$  smaller (6 orders of magnitude) than the decay widths into electrons. This result is mainly a consequence of the phase space [36], which is strongly suppressed for muons [36]. The range of integration of  $q$  in the cases of muons is [0.211, 0.215] GeV. Notice in this respect that, the calculation of the  $\Xi^*$  di-muon decays requires a value of  $W = 1.533$  GeV, between the values of  $W$  displayed in Fig. 3.

Our estimates are compatible with the estimates from Xu *et al.* [36] for the  $\Delta \rightarrow \mu^+\mu^-N$  and  $\Sigma^{*0} \rightarrow \mu^+\mu^-\Lambda$

Decay	$\text{BR}(\gamma B)$	$\text{BR}(e^+e^-B)$	$\text{BR}(\mu^+\mu^-B)$
$\Delta \rightarrow \ell^+\ell^-N$	$0.54 \times 10^{-2}$	$4.4 \times 10^{-5}$	$3.1 \times 10^{-7}$
$\Sigma^{*0} \rightarrow \ell^+\ell^-\Lambda$	$1.25 \times 10^{-2}$	$8.4 \times 10^{-5}$	$2.7 \times 10^{-7}$
$\Sigma^{*+} \rightarrow \ell^+\ell^-\Sigma^+$	$0.69 \times 10^{-2}$	$3.0 \times 10^{-5}$	
$\Sigma^{*0} \rightarrow \ell^+\ell^-\Sigma^0$	<b><math>0.086 \times 10^{-2}</math></b>	$6.1 \times 10^{-6}$	
$\Sigma^{*-} \rightarrow \ell^+\ell^-\Sigma^-$	<b><math>0.0036 \times 10^{-2}</math></b>	$2.3 \times 10^{-7}$	
$\Xi^{*0} \rightarrow \ell^+\ell^-\Xi^0$	<b><math>1.89 \times 10^{-2}</math></b>	$1.4 \times 10^{-4}$	$2.1 \times 10^{-10}$
$\Xi^{*-} \rightarrow \ell^+\ell^-\Xi^-$	<b><math>0.023 \times 10^{-2}</math></b>	$1.8 \times 10^{-6}$	$2.8 \times 10^{-12}$

TABLE VII. Summary of branching ratios. The results in boldface for  $\text{BR}(\gamma B)$  are based on the estimates of the present model.

decays. Also for the cascades, we obtain estimates consistent with Ref. [36], within their large error bars.

### F. Summary of Dalitz dilepton decays

In Table VII, we summarize our knowledge of radiative, di-electron and di-muon decays, in terms of the branching ratios. The last four radiative decays are estimated based on our own calculations for the magnetic form factor (indicated in boldface).

The results from Table VII allow us to compare the magnitudes of the branching ratios and discuss the expectations of measurements in future experiments. Our calculations indicate that the  $\Xi^{*0} \rightarrow e^+e^-\Xi^0$  decay has the largest branching ratio ( $\sim 10^{-4}$ ) followed by the  $\Delta$ ,  $\Sigma^{*0} \rightarrow e^+e^-\Lambda$  and  $\Sigma^{*+}$  decays (branching ratios  $\sim 10^{-5}$ ). The  $\Sigma^{*0} \rightarrow e^+e^-\Sigma^0$  and  $\Xi^{*-}$  decays have branching ratios of the order  $10^{-6}$ . The last result shows that the  $\Xi^{*-}$  Dalitz decay, suppressed in the exact  $SU(3)$  symmetry, has a branching ratio just an order of magnitude below the  $\Sigma^{*+} \rightarrow e^+e^-\Sigma^+$  decay. The last decay is expected to be observed in a near future [10]. Only the  $\Sigma^{*-}$  decay has reduced branching ratio ( $\sim 10^{-7}$ ).

As for the di-muon Dalitz decays, the  $\Delta$  and  $\Sigma^{*0} \rightarrow \mu^+\mu^-\Lambda$  decays have branching ratios of the order of  $10^{-7}$ , only 2 orders of magnitude below the measured  $\Delta(1232)$  Dalitz decay width at HADES, and the HADES/PANDA feasibility study for  $\Sigma^{*0} \rightarrow e^+e^-\Lambda$  [9, 10].

With the possibility of creation of a large number of baryons with strange quarks at HADES, PANDA, BESIII, and LHCb, one can expect to measure in a near future di-electron Dalitz decay widths for the decays  $\Sigma^{*0} \rightarrow \Lambda$ ,  $\Sigma^{*+} \rightarrow \Sigma^+$ ,  $\Sigma^{*0} \rightarrow \Sigma^0$ ,  $\Xi^{*0} \rightarrow \Xi^0$  and  $\Xi^{*-} \rightarrow \Xi^-$ , as well as di-muon Dalitz decay widths for the  $\Delta \rightarrow N$  and  $\Sigma^{*0} \rightarrow \Lambda$  transitions.

## VIII. OUTLOOK AND CONCLUSIONS

Most of the experimental studies about the electromagnetic structure of the baryons have been performed in the spacelike region. Only recently, the access to the timelike region of the baryon transitions ( $\gamma^*B \rightarrow B'$ ) became possible in *direct* electromagnetic transitions with the measurement of the  $\Delta(1232)$  di-electron Dalitz decay width at HADES. Measurements of baryon radiative decays and Dalitz decays are very important for our understanding of the internal structure of nucleon resonances and hyperons.

The characteristics of the HADES and PANDA facilities indicate that measurements of Dalitz di-electron decays of nucleon resonances and hyperons can be measured at GSI in the near future. There is also the expectation based on the estimated branching ratios that measurements of baryon Dalitz di-muon decays may be observed in facilities such as BESIII and LHCb.

From the possible electromagnetic decays of decuplet baryons into octet baryons, only three radiative decays are known presently:  $\Delta(1232) \rightarrow \gamma N$ ,  $\Sigma^0(1385) \rightarrow \gamma\Lambda(1116)$ , and  $\Sigma^+(1385) \rightarrow \gamma\Sigma^+(1193)$ . The present work suggests, based on the estimated magnitudes and improvement of the experimental conditions, that the  $\Xi^0(1530) \rightarrow \gamma\Xi^0(1318)$  and  $\Sigma^0(1385) \rightarrow \gamma\Sigma^0(1193)$  decays can be measured in the next few years. There is also the possibility that the  $\Sigma^-(1385) \rightarrow \gamma\Sigma^-(1193)$  decay, forbidden in the case that the exact  $SU(3)$  flavor symmetry holds, may also be measured soon due to the closeness of the estimated result with the present experimental limit. We may also expect observations of the  $\Xi^-(1530) \rightarrow \gamma\Xi^-(1318)$  decay due to the similarities with the  $\Sigma^-(1385) \rightarrow \gamma\Sigma^-(1193)$  decay.

From the feasibility studies of Dalitz di-electron decays at HADES and PANDA and the progress in the measurements of the decuplet baryon radiative decays, one may expect that the  $\Sigma^0(1385) \rightarrow e^+e^-\Lambda(1116)$ ,  $\Sigma^+(1385) \rightarrow e^+e^-\Sigma^+(1193)$  and  $\Xi^0(1530) \rightarrow e^+e^-\Xi^0(1318)$  decays will be measured soon at HADES and PANDA. The estimated magnitudes of the branching ratios suggest also that the  $\Delta(1232)$  and  $\Sigma^0(1385) \rightarrow \Lambda(1116)$  decays into di-muons may be measured at BESIII or LHCb.

In the present work, we study the role of the meson cloud on the octet baryon to decuplet baryon transition form factors, with particular focus on the kaon cloud, which is more relevant to baryons with strange quarks. This effect could in principle be studied in the spacelike region. In the spacelike region, however, our knowledge is restricted to the  $\gamma^*N \rightarrow \Delta(1232)$  transition, which manifests a very weak dependence on the kaon cloud, since the non-valence contributions are dominated by the pion cloud processes. In these conditions the impact of the kaon cloud can be better seen on the transition form factors related to the decuplet baryons  $\Sigma(1385)$  and  $\Xi(1530)$ . We conclude that the kaon cloud can enhance the estimates of the  $\Sigma(1385)$  radiative decays in about 27% and the  $\Xi(1530)$  radiative

decays in about 50%. We focus also our interest in the  $q^2$  dependence of the form factors with impact on the Dalitz decay widths. We conclude that the  $q^2$  dependence of the form factors may be more relevant for the  $\Sigma^0(1385) \rightarrow \Lambda(1116)$ , and  $\Sigma^+(1385) \rightarrow \Sigma^+(1193)$  transitions. As for the  $\Sigma^{0,-}(1385) \rightarrow \Sigma^{0,-}(1193)$  and  $\Xi^{0,-}(1530) \rightarrow e^+e^-\Xi^{0,-}(1318)$ , we conclude that the  $q^2$  dependence is not relevant for the calculation of the Dalitz di-electron decay widths.

The final conclusion is that the present estimates may be used to guide the experimental studies of baryon Dalitz decays, and that our predictions may be tested soon at HADES, PANDA or other facilities. The formalism used in the present work may be used in future theoretical studies, extending the  $SU(3)$  flavor sector (quarks  $u$ ,  $d$  and  $s$ ) with the inclusion of the heavy quarks  $c$  or  $b$ . Within this extension it will be possible to calculate radiative and Dalitz decays of baryons with heavy quarks.

## ACKNOWLEDGMENTS

The authors acknowledge the support and warm hospitality of APCTP (Asia Pacific Center for Theoretical Physics) during the Workshop (APCTP PROGRAMS 2023) "Origin of Matter and Masses in the Universe: Hadrons in free space, dense nuclear medium, and compact stars", where important discussions and development were achieved on the topic. K. T. thanks the OMEG (Origin of Matter and Evolution of Galaxies) Institute at Soongsil University for the supports in many aspects during the collaboration visit in Korea. G. R. thanks to the LFTC group of the Universidade Cruzeiro do Sul and Universidade Cidade de São Paulo for their hospitality during the visit in February of 2023. G. R. was supported the Basic Science Research Program through the National Research Foundation of Korea (NRF) funded by the Ministry of Education (Grant No. NRF-2021R1A6A1A03043957). K. T. was supported by Conselho Nacional de Desenvolvimento Científico e Tecnológico (CNPq, Brazil), Processes No. 313063/2018-4 and No. 426150/2018-0, and FAPESP Process No. 2019/00763-0, and his work was also part of the projects, Instituto Nacional de Ciência e Tecnologia - Nuclear Physics and Applications (INCT-FNA), Brazil, Process No. 464898/2014-5, and FAPESP Temático, Brazil, Process No. 2017/05660-0.

## Appendix A: Quark form factors

Motivated by the VMD mechanism, we use the following parametrization for the quark form factors  $f_{i0}$  and

$f_{i\pm}$  ( $i = 1, 2$ ):

$$f_{1+}(q^2) = \lambda_q + (1 - \lambda_q) \frac{m_\omega^2}{m_\omega^2 - q^2} - c_+ \frac{M_h^2 q^2}{(M_h^2 - q^2)^2}, \quad (\text{A1})$$

$$f_{1-}(q^2) = \lambda_q + (1 - \lambda_q) \frac{m_\rho^2}{m_\rho^2 - q^2} - c_- \frac{M_h^2 q^2}{(M_h^2 - q^2)^2}, \quad (\text{A2})$$

$$f_{10}(q^2) = \lambda_q + (1 - \lambda_q) \frac{m_\phi^2}{m_\phi^2 - q^2} - c_0 \frac{M_h^2 q^2}{(M_h^2 - q^2)^2}, \quad (\text{A3})$$

$$f_{2+}(q^2) = \kappa_+ \left\{ d_+ \frac{m_\omega^2}{m_\omega^2 - q^2} + (1 - d_+) \frac{M_h^2}{M_h^2 - q^2} \right\}, \quad (\text{A4})$$

$$f_{2-}(q^2) = \kappa_- \left\{ d_- \frac{m_\rho^2}{m_\rho^2 - q^2} + (1 - d_-) \frac{M_h^2}{M_h^2 - q^2} \right\}, \quad (\text{A5})$$

$$f_{20}(q^2) = \kappa_0 \left\{ d_0 \frac{m_\phi^2}{m_\phi^2 - q^2} + (1 - d_0) \frac{M_h^2}{M_h^2 - q^2} \right\}, \quad (\text{A6})$$

where  $m_\rho$ ,  $m_\omega$ , and  $m_\phi$  represent the masses of the mesons  $\rho$ ,  $\omega$ , and  $\phi$ , respectively. The terms with  $M_h$  correspond to an effective heavy vector meson which parametrize the short range effects. The value of  $M_h$  is fixed as  $M_h = 2M_N$  [48, 74]. In the calculations, we use the approximation  $m_\omega = m_\rho$  for simplicity. We use the values  $m_\rho = 0.771$  GeV as discussed in Appendix B and  $m_\phi = 1.020$  GeV.

In Eqs. (A4)–(A6),  $\kappa_\pm$  represent the isoscalar/isovector quark anomalous magnetic moments, and  $\kappa_0$  is the strange quark anomalous magnetic moment. We use the parametrization derived from the studies of the octet and decuplet baryons [49, 75]. We take in particular  $\kappa_- = 1.435$ ,  $\kappa_+ = 1.803$ , and  $\kappa_0 = 1.462$ . To convert to the flavors  $q = u, d, s$ , one uses the following relations:  $\kappa_u = \frac{1}{4}(\kappa_+ + 3\kappa_-)$ ,  $\kappa_d = \frac{1}{2}(2\kappa_- - \kappa_+)$ , and  $\kappa_s = \kappa_0$  [48, 49].

In Eqs. (A1)–(A3),  $\lambda_q$  is a parameter related to the quark density number in deep inelastic scattering [48]. The numerical value is  $\lambda_q = 1.21$ . The remaining parameters are  $c_+ = 4.160$ ,  $c_- = 1.160$ ,  $c_0 = 4.427$ ,  $d_+ = d_- = -0.686$ , and  $d_0 = -1.860$  [49, 75].

The expressions (A1)–(A6) are valid in the region  $q^2 < 0$ , when the vector meson decay widths vanish,  $\Gamma_v \equiv 0$  ( $v = \rho, \omega, \phi$ ). For the extension of the quark form factors to the timelike region ( $q^2 > 0$ ), we consider the replacement ( $v = \rho, \omega, \phi$ )

$$\frac{m_v^2}{m_v^2 - q^2} \rightarrow \frac{m_v^2}{m_v^2 - q^2 - im_v \Gamma_v(q^2)}. \quad (\text{A7})$$

The decay width functions  $\Gamma_v(q^2)$ , which describe the dressing of the vector mesons in terms of the possible meson decay channels, are discussed next.

For the  $\rho$  meson (isovector component) the decay width parametrizes the width associated with the decay  $\rho \rightarrow 2\pi$  for a virtual  $\rho$  with square four-momentum  $q^2$ . This function can be expressed as in Eq. (5.3), due to the connection with the pion electromagnetic form factor [111].

As for the isoscalar channel, associated with the  $\omega$  meson, one needs to consider the combination of the decays

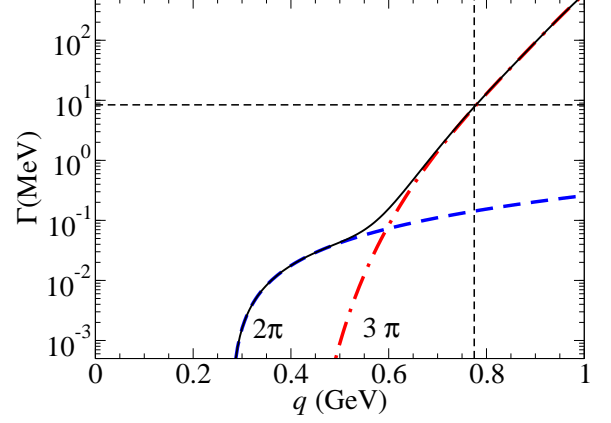


FIG. A.1. Function  $\Gamma_\omega$  versus  $q$ . The solid line represents the sum of the two channels. The short-dashed vertical and horizontal lines indicate, respectively, the  $\omega$  mass point and the  $\omega$ -physical width (8.4 MeV).

$\omega \rightarrow 2\pi$  and  $\omega \rightarrow 3\pi$ . Following our work on the  $N(1520)$  Dalitz decay [25], we decompose

$$\Gamma_\omega(q^2) = \Gamma_{2\pi}(q^2) + \Gamma_{3\pi}(q^2), \quad (\text{A8})$$

where the first term parametrizes the decay  $\omega \rightarrow 2\pi$  and the second term parametrizes the decay  $\omega \rightarrow 3\pi$ . The expression for  $\Gamma_{2\pi}(q^2)$  is similar to  $\Gamma_\rho(q^2)$  except for the strength [25, 126]. For the decay  $\omega \rightarrow 3\pi$ , we consider a model based on the process  $\omega \rightarrow \rho\pi \rightarrow 3\pi$ , where the intermediate  $\rho$  decays into two pions [126]. We do not write down here the expressions for  $\Gamma_{2\pi}$  and  $\Gamma_{3\pi}$ , since they can be found in Ref. [25], except for the expression for  $\Gamma_{2\pi}(q^2)$  where we use the factor  $\frac{m_\omega}{\sqrt{q^2}}$  instead of  $\frac{m_\rho}{q^2}$  and replace the  $\pi\rho$  coupling from  $g' = 10.6$  MeV to  $g' = 13.86$  MeV, in order to reproduce  $\Gamma_{3\pi}(m_\omega^2) = 7.6$  MeV [25]. The numerical results for the function  $\Gamma_\omega(q^2)$  are presented in Fig. A.1.

Finally, for the  $\phi$  decay width, we consider the simplified parametrization,

$$\Gamma_\phi(q^2) = \Gamma_\phi^0 \frac{m_\phi}{\sqrt{q^2}} \left( \frac{q^2 - 4m_K^2}{m_\phi^2 - 4m_K^2} \right)^{3/2} \theta(q^2 - 4m_K^2), \quad (\text{A9})$$

where  $\Gamma_\phi^0 = 4.23 \times 10^{-3}$  GeV, and  $m_K$  is the kaon mass ( $m_K \simeq 0.5$  GeV). Equation (A9) describes the  $\phi \rightarrow 2K$  ( $K$  is the kaon) under the assumption that it is the dominant decay of the  $\phi$ . According to PDG  $\phi$  decays predominantly on  $2K$  (49%) and  $K_S^0 K_L^0$  (34%) [21].

For the range of the calculation of the present work ( $W < 2$  GeV) the regularization of the  $\phi$  pole is not very relevant, since  $m_\phi^2 \simeq 1$  GeV<sup>2</sup>  $\gg$   $q^2$ . The singularities associated with the  $\phi$  meson appear, then only for  $W \geq M_B + m_\phi > 2.1$  GeV.

## Appendix B: Parametrization of the pion cloud contribution

We discuss here the pion cloud parametrization (5.1) and the function (5.2). We fit the function  $|F_\pi(q^2)|^2$  to the data of respective regions of spacelike [127] and timelike [128].

Since we focus on the isovector component of  $F_\pi(q^2)$  ( $\rho \rightarrow \pi\pi$ ), we do not expect an exact description near the peak due to the overlap of the data with the isoscalar component ( $\omega \rightarrow \pi\pi$ ). In order to optimize a description of lower  $q^2$  region (below the peak) and also to avoid the contamination by the excited states of the  $\rho$ , we restrict the fit to the  $q^2 < 0.8 \text{ GeV}^2$  data. The parameters associated with the best fit are presented in Eq. (5.4). The comparison with the spacelike and timelike data [127, 128] is presented in Fig. B.1.

One can notice in Fig. B.1 that the parametrization (5.2) does not provide a high quality description of the  $q^2 > 0$  data, since there is some underestimation of the data on the left side of the peak. We recall that, as discussed in Sec. V A, additional shape parameters are necessary to obtain a more accurate description of the  $|F_\pi(q^2)|^2$  data [117, 119, 120].

For the present study, it is important to ensure that one has an accurate description of the spacelike region and that the parametrization has the correct analytic behavior near the two pion threshold, as well as for very large  $Q^2 = -q^2$ . Minor deviations on the timelike region are not relevant since the meson cloud contributions provide in general small corrections to the dominant valence quark contributions.

One can now focus on Eq. (5.1). Following previous studies on the  $\gamma^*N \rightarrow \Delta(1232)$  transition [14, 15] we consider a parametrization of the pion cloud contribution given by the combination of the two terms: a term associated with the direct coupling with the pion and a term associated with the coupling with the intermediate baryon states (see Fig. 1).

The second term is discussed in the main text and includes the function  $\tilde{G}_D$  regulated by the cutoff  $\Lambda_D^2 = 0.9 \text{ GeV}^2$  determined in a previous work [14].

The first term includes a tripole factor with a cutoff  $\Lambda_\pi^2$ . The cutoff  $\Lambda_\pi^2$  measures the falloff of the pion cloud contribution of the diagram (a) to the magnetic transition form factor. It can be determined in the case of the  $\gamma^*N \rightarrow \Delta(1232)$  transition, directly from the comparison with the physical data. Since the valence quark contribution is well calibrated by the comparison with the lattice data with heavy quarks, the pion cloud contributions can be determined by the combination of the two terms of (5.1) with the bare contribution, where  $\Lambda_\pi^2$  is adjusted to the data. We obtain a very good description of the data with  $\Lambda_\pi^2 = 2.30 \text{ GeV}^2$ . The comparison with the data is presented in Fig. B.2. Notice that in the figure we consider only the pion cloud contribution. The small kaon cloud contribution is not included.

## Appendix C: Meson cloud contributions

In this appendix, we present the general expressions for the meson cloud contributions associated with the diagrams (a) and (b) in Fig. 1. The analytic results for the expansion in terms of  $Q^2$  are presented in Appendix D.

The expressions presented next are derived from the cloudy bag model (CBM) formalism [102–106], where the formulas are derived in the heavy baryon limit, by neglecting the three-momentum of the baryons in the meson cloud loops.

The calculation of the contributions associated with the diagrams (a) and (b) from Fig. 1 requires the evaluation of integrals of the form [103–106],

$$H_{B'B_1B_1}^M = \frac{f_{MB'B_1}f_{MB_1B}}{m_\pi^2} \int \frac{d^3\mathbf{k}}{(2\pi)^3} F_a(B', B_1, B; M),$$

$$H_{B'B_1B_2B_1}^{2M} = \frac{f_{MB'B_2}f_{MB_1B}}{m_\pi^2} \int \frac{d^3\mathbf{k}}{(2\pi)^3} F_b(B', B_2, B_1, B; M),$$

where a and b label the CBM integrand functions associated with the two diagrams. The particle labels ( $B, B', B_1, B_2$  and  $M$ ) include the reference to the three-momentum of the particles.

The factors  $f_{MB_1B_2}$  represent the  $MB_1B_2$  couplings determined by the  $SU(3)$  symmetry. The factor  $1/m_\pi^2$  is included by convenience taking into account the ratios between kaon, eta and pion masses, factored in the functions  $F_a$  and  $F_b$ . Using the relations  $f_{MB_1B_2}$  with the  $\pi NN$  coupling  $f \equiv f_{\pi NN}$ , we can express the product of the meson-baryon coupling constants in terms of a flavor coefficient and the factor  $f^2/m_\pi^2$  [103–106]. In summary, the integrals can be written as a product of a flavor coefficient,  $f^2/m_\pi^2$  and an explicit integral, independent of the coupling factors.

To represent the loop integrals, we use the notation,

$$\omega_{\mathbf{k}} = \sqrt{m^2 + \mathbf{k}^2} \quad (C1)$$

$$\omega_{B_2B_1} = M_{B_2} - M_{B_1}, \quad (C2)$$

where  $m$  is the mass of the meson and  $M_{B_i}$  is the mass of the baryon  $B_i$  ( $i = 1, 2$ ). For the case  $\mathbf{q} \neq \mathbf{0}$ , we need also the auxiliary functions,

$$\omega_{\pm} = \sqrt{m^2 + (\mathbf{k} \pm \frac{1}{2}\mathbf{q})^2}, \quad (C3)$$

and

$$\mathbf{k}_{\pm} = |\mathbf{k} \pm \frac{1}{2}\mathbf{q}|. \quad (C4)$$

Using the decomposition in polar coordinates with the symmetry in terms of the direction of  $\mathbf{q}$ , one obtains the relation

$$\int \frac{d^3\mathbf{k}}{(2\pi)^3} \equiv \frac{1}{4\pi^2} \int_0^{+\infty} k^2 dk \int_{-1}^1 dz, \quad (C5)$$

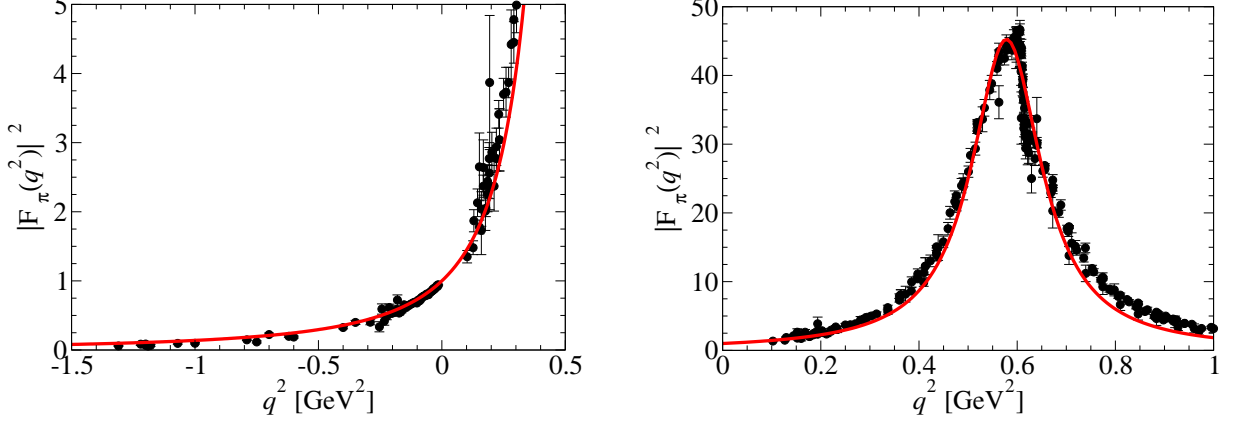


FIG. B.1. Comparison of the best fit (5.2) with the spacelike (left panel) and timelike (right panel)  $|F_\pi(q^2)|^2$  data [127, 128]. The parameters associated with the best fit are  $m_\rho = 0.771$  GeV and  $\Gamma_\rho^0 = 0.117$  GeV.

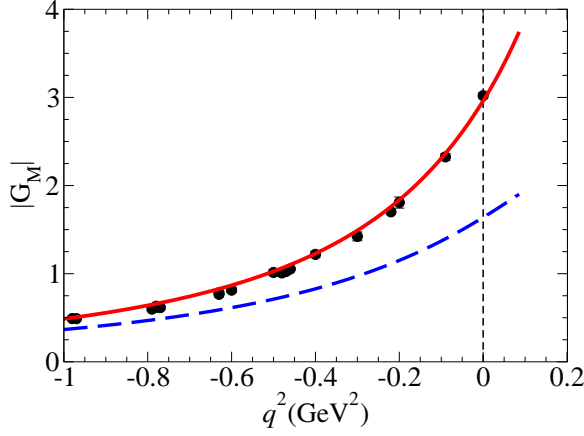


FIG. B.2. Results from the covariant spectator quark model for  $|G_M(q^2, M_\Delta)|$  relative to the  $\gamma^* N \rightarrow \Delta$  transition (solid line). The valence and pion cloud contributions are combined according to Eq. (3.1). The data are from Refs. [121, 129]. The dashed line is the contribution from the core (valence quarks).

where  $z = \cos \theta$  and  $k \equiv |\mathbf{k}|$  ( $\theta$  is the angle between  $\mathbf{k}$  and  $\mathbf{q}$ ). When the integration in  $z$  is analytic, we can express the final expression in terms of the radial variable  $k$ .

The CBM vertex form factor  $\mathcal{U}(kR)$  is represented by [102–106]

$$\mathcal{U}(kR) = j_0(kR) + j_2(kR), \quad (\text{C6})$$

where  $j_0$  and  $j_2$  are spherical Bessel functions of the first kind.  $R$  is the bag radius ( $R \simeq 1$  fm). In the following, we use  $u = kR$ .

In the present case we need to expand the meson cloud contributions up to the first order of  $Q^2$  (second order in  $u$ ), which is sufficient for the present purpose of estimating in the small- $Q^2$  region. Then, one can use the

following expansion for  $u = kR$ :

$$\begin{aligned} \mathcal{U}(\sqrt{u^2 + h}) &= \mathcal{U}(u) + \frac{\mathcal{U}'(u)}{2u} h \\ &+ \frac{1}{4} \left[ \frac{\mathcal{U}''(u)}{u^2} - \frac{\mathcal{U}'(u)}{u^3} \right] \frac{h^2}{2} + \mathcal{O}(h^3). \end{aligned} \quad (\text{C7})$$

To simplify the final expressions, we use the compact notation,

$$\mathcal{U}(\sqrt{(kR)^2 + h}) \simeq \mathcal{U}(kR) \left[ 1 + g_1 h + g_2 \frac{h^2}{2} \right], \quad (\text{C8})$$

where

$$g_1 = \frac{1}{2kR} \frac{\mathcal{U}'(kR)}{\mathcal{U}(kR)}, \quad (\text{C9})$$

$$g_2 = \frac{1}{4\mathcal{U}(kR)} \left[ \frac{\mathcal{U}''(kR)}{(kR)^2} - \frac{\mathcal{U}'(kR)}{(kR)^3} \right]. \quad (\text{C10})$$

### 1. Diagram (a)

The contributions from the diagram (a) for the  $\gamma^* B \rightarrow B'$  can be written as

$$G_M^{\text{MC}a}(Q^2) = \sum_{M, B_1} C_{B'B; B_1}^M H_{B'B; B_1}^M(Q^2), \quad (\text{C11})$$

where  $C_{B'B; B_1}^M$  are the coefficients calculated in the CBM framework.

In Table D1, we present the reduced matrix elements  $G_M^{\text{MC}a}$  for the kaon cloud contributions. To obtain the contributions of the different components of the  $\Sigma^* \rightarrow \gamma \Sigma$  transitions, we replace the operators  $J_3$  (isospin 1) by the charge of the  $\Sigma$  (+, 0, -). As for the  $\Xi^* \rightarrow \gamma \Xi$  transitions, we replace  $\tau_3$  (isospin 1/2) by the  $\Xi$  isospin projection ( $\Xi^0$  when  $\tau_3 \rightarrow +1$ ;  $\Xi^-$  when  $\tau_3 \rightarrow -1$ ).

$G_M^{Ka}$	
$\gamma^* N \rightarrow \Delta$	$\frac{4\sqrt{2}}{9}(2M_N) \left[ \frac{1}{25}H_\Sigma^K + \frac{1}{5}H_{\Sigma^*}^K \right]$
$\gamma^* \Lambda \rightarrow \Sigma^{0*}$	$\frac{2\sqrt{2}}{15\sqrt{3}}(2M_\Lambda) \left[ \frac{3}{5}H_N^K - \frac{1}{5}H_\Xi^K + 2H_{\Xi^*}^K \right]$
$\gamma^* \Sigma \rightarrow \Sigma^*$	$\frac{\sqrt{2}}{3}(2M_\Sigma) \left[ \frac{2}{75}H_N^K + \frac{8}{15}H_\Delta^K + \frac{2}{15}H_\Xi^K + \frac{4}{15}H_{\Xi^*}^K \right] +$ $\frac{\sqrt{2}}{3}(2M_\Sigma) \left[ -\frac{2}{75}H_N^K + \frac{4}{15}H_\Delta^K + \frac{2}{15}H_\Xi^K + \frac{4}{15}H_{\Xi^*}^K \right] J_3$
$\gamma^* \Xi \rightarrow \Xi^*$	$\frac{\sqrt{2}}{3}(2M_\Xi) \left[ -\frac{1}{25}H_\Lambda^K + \frac{1}{5}H_\Sigma^K + \frac{2}{5}H_{\Sigma^*}^K + \frac{2}{5}H_\Omega^K \right] +$ $\frac{\sqrt{2}}{3}(2M_\Xi) \left[ \frac{1}{25}H_\Lambda^K + \frac{1}{15}H_\Sigma^K + \frac{2}{15}H_{\Sigma^*}^K + \frac{2}{5}H_\Omega^K \right] \tau_3$

TABLE D1. Kaon cloud contributions  $G_M^K$  for the diagram (a). For simplicity, we use  $H_{B_1}^K$  to represent  $H_{B'B_1}^K$ , since the states  $B'$  and  $B$  are evident. In addition to the results presented above, the proper isospin factors are included for the  $\Sigma^{*\pm,0}$ ,  $\Sigma^{\pm,0}$ ,  $\Xi^{*0,-}$  and  $\Xi^{0,-}$  in the final isospin (charge) dependent results in Tables III and IV.

As discussed in the main text, the integrals  $H_{B'B_1}^M$  are evaluated in the Breit frame. We can characterize the diagram (a) with the momenta  $\mathbf{k} - \frac{1}{2}\mathbf{q}$  and  $\mathbf{k} + \frac{1}{2}\mathbf{q}$  for the first and second meson lines and a momentum  $-\mathbf{k}$  for the intermediate baryon ( $B_1$ ). The CBM integrals depend only on the three-momentum of the intermediate state particles. The explicit form is

$$H_{B'B_1}^M(Q^2) = \frac{f^2}{m_\pi^2} \int \frac{d^3\mathbf{k}}{(2\pi)^3} \frac{\mathcal{U}(\mathbf{k}_+R)\mathcal{U}(\mathbf{k}_-R)}{4\omega_+\omega_- \left[ (\omega_+ + \omega_-)^2 - \omega_{B'}^2 \right]} \frac{(\hat{\mathbf{q}} \times \mathbf{k})^2}{4} \mathcal{G}_a, \quad (\text{C12})$$

where

$$\mathcal{G}_a = \frac{2(\omega_+ + \omega_-)(\omega_{B_1B} + \omega_+ + \omega_-) + 2\omega_{BB'}\omega_+}{(\omega_{B_1B'} + \omega_+)(\omega_{B_1B} + \omega_-)} + \frac{2(\omega_+ + \omega_-)(\omega_{B_1B} + \omega_+ + \omega_-) + 2\omega_{BB'}\omega_-}{(\omega_{B_1B'} + \omega_-)(\omega_{B_1B} + \omega_+)}. \quad (\text{C13})$$

In Eq. (C12), the factor  $(\hat{\mathbf{q}} \times \mathbf{k})^2 = \mathbf{k}^2 \sin^2\theta$  represents the  $p$ -wave contributions of the mesons in the meson cloud loops [107, 108]. The presence of the last factor makes it difficult to take the limit  $\mathbf{q}^2 = 0$ . One needs then to perform the angular integration before taking the limit. The result of the expansion in terms of  $Q^2$  is presented in Appendix D.

## 2. Diagram (b)

The  $\gamma^* B \rightarrow B'$  meson cloud contributions from the diagram (b) can be expressed in the form

$$G_M^{\text{MC}b}(Q^2) = \sum_{M, B_1, B_2} D_{B'B_2B_1}^M H_{B'B_2B_1}^{2M}(Q^2). \quad (\text{C14})$$

The coefficients  $D_{B'B_2B_1}^M$  are calculated using the CBM. The results for the reduced matrix elements  $G_M^{\text{MC}b}$

are presented in Table D2. We use the same convention to  $J_3$  and  $\tau_3$  as in Table D1.

The coefficients  $D_{B'B_2B_1}^M$  include the interaction of the meson with the bare cores, which depend on valence quark contributions. Those contributions can be expressed in terms of the quark effective magnetic moments  $\mu_q$ , as defined in Refs. [37, 76]. In the exact  $SU(2)$  symmetric limit for the meson cloud ( $\mu_u = \mu_d$ ), the coefficients depend only on  $\mu_s$  and the average of  $u$  and  $d$  magnetic moments

$$\bar{\mu}_u = (2\mu_u + \mu_d)/3. \quad (\text{C15})$$

To write the final expressions, we use the notation,

$$\begin{aligned} \mu_S &= \frac{1}{3}(\bar{\mu}_u + 2\mu_s), & \mu_V &= \bar{\mu}_u, \\ \mu_1 &= \frac{1}{3}(2\bar{\mu}_u + \mu_s), & \mu_2 &= \bar{\mu}_u - \mu_s, \\ \mu_3 &= \frac{1}{9}(\bar{\mu}_u + 8\mu_s), & \mu_4 &= \frac{1}{3}(-\bar{\mu}_u + 4\mu_s). \end{aligned} \quad (\text{C16})$$

In this case, we can use a configuration where the momentum of  $B_1$  is  $\mathbf{k}$ , the momentum of  $B_2$  is  $\mathbf{k} + \mathbf{q}$  and the momentum of the meson is  $-(\mathbf{k} + \frac{1}{2}\mathbf{q})$ . The explicit form is

$$H_{B'B_2B_1}^{2M}(Q^2) = \frac{f^2}{m_\pi^2} \int \frac{d^3\mathbf{k}}{(2\pi)^3} \frac{k_+^2 [\mathcal{U}(\mathbf{k}_+R)]^2}{2\omega_+(\omega_{B_2B'} + \omega_+)(\omega_{B_1B} + \omega_+)}. \quad (\text{C17})$$

The result of the expansion in terms of  $Q^2$  is presented in Appendix D. For more details about Eqs. (C11) and (C14) see Ref. [37].

## Appendix D: Calculation of $G_M^{K\ell}(0)$ and $\frac{dG_M^{K\ell}}{dQ^2}(0)$

In this appendix, we present the final expressions for the kaon cloud contributions in the limit  $Q^2 = 0$ ,  $G_M^{K\ell}(0)$ ,

$G_M^{Kb}$	
$\gamma^* N \rightarrow \Delta$	$\frac{2\sqrt{2}}{3}\mu_V \left[ \frac{4}{25}H_{\Sigma\Lambda}^{2K} + \frac{1}{5}H_{\Sigma^*\Lambda}^{2K} + \frac{8}{225}H_{\Sigma\Sigma}^{2K} + \frac{4}{45}H_{\Sigma^*\Sigma^*}^{2K} - \frac{1}{45}H_{\Sigma^*\Sigma}^{2K} + \frac{4}{225}H_{\Sigma\Sigma^*}^{2K} \right]$
$\gamma^* \Lambda \rightarrow \Sigma^{0*}$	$\sqrt{\frac{2}{3}}\frac{M_\Lambda}{M_N}\mu_V \left[ \frac{4}{15}H_{\Lambda N}^{2K} + \frac{8}{15}H_{\Delta N}^{2K} + \frac{4}{225}H_{\Xi\Xi}^{2K} + \frac{4}{45}H_{\Xi^*\Xi}^{2K} + \frac{8}{225}H_{\Xi\Xi^*}^{2K} + \frac{8}{45}H_{\Xi^*\Xi^*}^{2K} \right]$
$\gamma^* \Sigma \rightarrow \Sigma^*$	$\frac{\sqrt{2}}{3}\frac{M_\Sigma}{M_N}\mu_S \left[ \frac{4}{9}H_{\Xi^*\Xi}^{2K} - \frac{8}{225}H_{\Xi\Xi^*}^{2K} \right] + \frac{\sqrt{2}}{3}\frac{M_\Sigma}{M_N}\mu_3 \frac{4}{15}H_{\Xi\Xi}^{2K} + \frac{\sqrt{2}}{3}\frac{M_\Sigma}{M_N}\mu_V \left[ \frac{4}{225}H_{\Lambda N}^{2K} + \frac{16}{45}H_{\Delta\Delta}^{2K} \right] + \frac{\sqrt{2}}{3}\frac{M_\Sigma}{M_N}\mu_4 \frac{8}{45}H_{\Xi^*\Xi^*}^{2K} + \frac{\sqrt{2}}{3}\frac{M_\Sigma}{M_N}\mu_V \left[ \frac{4}{45}H_{\Lambda N}^{2K} - \frac{4}{45}H_{\Delta N}^{2K} + \frac{16}{225}H_{\Lambda\Delta}^{2K} + \frac{8}{9}H_{\Delta\Delta}^{2K} + \frac{4}{45}H_{\Xi\Xi}^{2K} + \frac{4}{9}H_{\Xi^*\Xi}^{2K} - \frac{8}{225}H_{\Xi\Xi^*}^{2K} - \frac{8}{45}H_{\Xi^*\Xi^*}^{2K} \right] J_3$
$\gamma^* \Xi \rightarrow \Xi^*$	$\frac{\sqrt{2}}{3}\frac{M_\Xi}{M_N}\mu_S \left[ \frac{2}{3}H_{\Sigma^*\Sigma}^{2K} - \frac{4}{75}H_{\Sigma\Sigma^*}^{2K} \right] + \frac{\sqrt{2}}{3}\frac{M_\Xi}{M_N}\mu_1 \frac{4}{15}H_{\Sigma\Sigma}^{2K} + \frac{\sqrt{2}}{3}\frac{M_\Xi}{M_N}\mu_s \left[ \frac{4}{75}H_{\Lambda\Lambda}^{2K} + \frac{8}{15}H_{\Omega\Omega}^{2K} \right] + \frac{\sqrt{2}}{3}\frac{M_\Xi}{M_N}\mu_2 \frac{8}{45}H_{\Sigma^*\Sigma^*}^{2K} + \frac{\sqrt{2}}{3}\frac{M_\Xi}{M_N}\mu_V \left[ -\frac{4}{75}H_{\Sigma\Lambda}^{2K} + \frac{2}{15}H_{\Sigma^*\Lambda}^{2K} + \frac{4}{15}H_{\Lambda\Sigma}^{2K} + \frac{16}{45}H_{\Sigma\Sigma}^{2K} + \frac{4}{9}H_{\Sigma^*\Sigma}^{2K} + \frac{4}{75}H_{\Lambda\Sigma^*}^{2K} - \frac{8}{225}H_{\Sigma\Sigma^*}^{2K} + \frac{16}{45}H_{\Sigma^*\Sigma^*}^{2K} \right] \tau_3$

TABLE D2. Kaon cloud contributions  $G_M^K$  for the diagram (b). For simplicity, we use  $H_{B_2B_1}^{2K}$  to represent  $H_{B'B_1B_2B_1}^{2K}$ , since the states  $B'$  and  $B$  are evident. In addition to the results presented above, the proper isospin factors are included for the  $\Sigma^{*\pm,0}, \Sigma^{\pm,0}, \Xi^{*0,-}$  and  $\Xi^{0,-}$  in the final isospin (charge) dependent results in Tables III and IV. The auxiliary factors  $\mu_V, \mu_S, \mu_i$  ( $i = 1, 2, 3, 4$ ) are defined by Eq. (C16).

and the result for  $\frac{dG_M^{K\ell}}{dQ^2}(0)$ . These results are used to calculate the cutoff parameters of the kaon cloud contributions associated with the diagrams (a) and (b), as described in Sec. VB. We use here the notation defined in Appendix C.

The kaon cloud contributions,  $G_M^{Ka}(Q^2)$  and  $G_M^{Kb}(Q^2)$  for the diagrams (a) and (b) are determined by Eqs. (C11) and (C14) for  $M = K$ . Since the coefficients  $C^K$  and  $D^K$  are known, and independent of  $Q^2$ , here we need to focus only on the integrals  $H^K$  and  $H^{2K}$ .

### 1. Diagram (a)

For small  $Q^2$ , we decompose the function  $H_{B'B_1}^M(Q^2)$  into two terms

$$H_{B'B_1}^K(Q^2) = H_{B'B_1}^{K(0)} + H_{B'B_1}^{K(1)}Q^2, \quad (D1)$$

where

$$H_{B'B_1}^{K(0)} = H_{B'B_1}^K(0), \quad H_{B'B_1}^{K(1)} = \frac{dH_{B'B_1}^K}{dQ^2}(0). \quad (D2)$$

To write the final results it is convenient to define the

variables

$$Z_1^a = \frac{\omega_{\mathbf{k}}}{\omega_{B_1B'} + \omega_{\mathbf{k}}} \frac{\omega_{\mathbf{k}}}{\omega_{B_1B} + \omega_{\mathbf{k}}}, \quad (D3)$$

$$Z_2^a = \left( \frac{\omega_{\mathbf{k}}}{\omega_{B_1B'} + \omega_{\mathbf{k}}} \right)^2 + \left( \frac{\omega_{\mathbf{k}}}{\omega_{B_1B} + \omega_{\mathbf{k}}} \right)^2 - Z_1^a, \quad (D4)$$

$$Z_3^a = \frac{\omega_{\mathbf{k}}}{\omega_{B_1B'} + \omega_{\mathbf{k}}} + \frac{\omega_{\mathbf{k}}}{\omega_{B_1B} + \omega_{\mathbf{k}}}, \quad (D5)$$

$$Z_4^a = \frac{\omega_{B_1B'} + \omega_{B_1B}}{4\omega_{\mathbf{k}} + \omega_{B_1B'} + \omega_{B_1B}}, \quad (D6)$$

$$Z_5^a = \frac{\omega_{B'B}^2}{4\omega_{\mathbf{k}} + \omega_{B_1B'} + \omega_{B_1B}} \frac{1}{\omega_{\mathbf{k}}} Z_1^a \quad (D7)$$

$$a_1 = \frac{4\omega_{\mathbf{k}}^2}{4\omega_{\mathbf{k}}^2 - \omega_{B'B}^2} + \frac{1}{2}Z_3^a + \frac{1}{2}Z_4^a, \quad (D8)$$

$$a_2 = 2 + Z_2^a + Z_5^a \quad (D9)$$

and the functions

$$G_a = \frac{(4\omega_{\mathbf{k}} + \omega_{B_1B'} + \omega_{B_1B})}{\omega_{\mathbf{k}}(\omega_{B_1B'} + \omega_{\mathbf{k}})(\omega_{B_1B} + \omega_{\mathbf{k}})} \times \frac{[\mathcal{U}(\mathbf{k}R)]^2}{4\omega_{\mathbf{k}}^2 - \omega_{B'B}^2}, \quad (D10)$$

$$A = \frac{1}{2}g_1(\mathbf{k}R)^2 + (g_2 - g_1^2)\frac{(\mathbf{k}R)^4}{5} - \frac{1}{5}(1 - a_1 - a_2)\frac{\mathbf{k}^4}{4\omega_{\mathbf{k}}^4} - a_1\frac{\mathbf{k}^2}{4\omega_{\mathbf{k}}^2}. \quad (D11)$$

The values of  $g_1$  and  $g_2$  are given by Eqs. (C9) and (C10).



Using the previous notation, we can write

$$H_{B'B;B_1}^{K(0)} = \frac{f^2}{m_\pi^2} \int_{\mathbf{k}} k^2 G_a, \quad (\text{D12})$$

$$H_{B'B;B_1}^{K(1)} = \frac{f^2}{m_\pi^2} \int_{\mathbf{k}} A G_a, \quad (\text{D13})$$

where

$$\int_{\mathbf{k}} \equiv \frac{1}{12\pi^2} \int_0^{+\infty} k^2 dk. \quad (\text{D14})$$

To calculate  $G_M^{K^a}(0)$ , we need to consider linear combinations of  $H_{B'B;B_1}^{K(0)}$  for the different intermediate states  $B_1$ , according to Eq. (C11). Similarly, the results for  $\frac{dG_M^{K^a}}{dQ^2}(0)$  are linear combinations of  $H_{B'B;B_1}^{K(1)}$  for the different intermediate states  $B_1$ . The numerical results for  $\frac{dG_M^{K^a}}{dQ^2}(0)/G_M^{K^a}(0)$  are presented in Table III.

## 2. Diagram (b)

Also for the diagram (b) we can decompose the function  $H_{B'B;B_2B_1}^{2K}(Q^2)$  for small  $Q^2$ ,

$$H_{B'B;B_2B_1}^{2K}(Q^2) = H_{B'B;B_2B_1}^{2K(0)} + H_{B'B;B_2B_1}^{2K(1)} Q^2, \quad (\text{D15})$$

where

$$\begin{aligned} H_{B'B;B_2B_1}^{2K(0)} &= H_{B'B;B_2B_1}^{2K}(0), \\ H_{B'B;B_2B_1}^{2K(1)} &= \frac{dH_{B'B;B_2B_1}^{2K}}{dQ^2}(0). \end{aligned} \quad (\text{D16})$$

To write the explicit expressions, we use

$$Z_1^b = \frac{\omega_{\mathbf{k}}}{\omega_{B_2B'} + \omega_{\mathbf{k}}} \frac{\omega_{\mathbf{k}}}{\omega_{B_1B} + \omega_{\mathbf{k}}}, \quad (\text{D17})$$

$$Z_2^b = \left( \frac{\omega_{\mathbf{k}}}{\omega_{B_2B'} + \omega_{\mathbf{k}}} \right)^2 + \left( \frac{\omega_{\mathbf{k}}}{\omega_{B_1B} + \omega_{\mathbf{k}}} \right)^2 + Z_1^b, \quad (\text{D18})$$

$$Z_3^b = 1 + \frac{\omega_{\mathbf{k}}}{\omega_{B_2B'} + \omega_{\mathbf{k}}} + \frac{\omega_{\mathbf{k}}}{\omega_{B_1B} + \omega_{\mathbf{k}}}. \quad (\text{D19})$$

and

$$G_b = \frac{[\mathcal{U}(kR)]^2}{2\omega_{\mathbf{k}}(\omega_{B_2B'} + \omega_{\mathbf{k}})(\omega_{B_1B} + \omega_{\mathbf{k}})}, \quad (\text{D20})$$

$$\begin{aligned} B &= \frac{1}{3}(g_2 + g_1^2)(kR)^4 + \frac{1}{6} \left( 7 - 2Z_3^b \frac{k^2}{\omega_{\mathbf{k}}^2} \right) g_1(kR)^2 \\ &+ \left( \frac{Z_3^b}{2} + \frac{Z_2^b}{3} \right) \frac{k^4}{4\omega_{\mathbf{k}}^4} - \frac{7}{6} Z_3^b \frac{k^2}{4\omega_{\mathbf{k}}^2} + \frac{1}{4}. \end{aligned} \quad (\text{D21})$$

Using the previous notation, we can write

$$H_{B'B;B_2B_1}^{2K(0)} = \frac{f^2}{m_\pi^2} \int_{\mathbf{k}} k^2 G_b, \quad (\text{D22})$$

$$H_{B'B;B_2B_1}^{2K(1)} = \frac{f^2}{m_\pi^2} \int_{\mathbf{k}} B G_b, \quad (\text{D23})$$

where the integral symbol is defined by Eq. (D14).

The final results for  $\frac{dG_M^{K^b}}{dQ^2}(0)/G_M^{K^b}(0)$  are presented in Table III.

## 3. Numerical calculation of $G_M^{K^a}(0)$ and $G_M^{K^b}(0)$

The calculations presented in this work are based on the numerical results for  $G_M^{K^a}(0)$  and  $G_M^{K^b}(0)$ , and the corresponding derivatives in the limit  $Q^2 = 0$ , presented in this appendix.

Compared to the results obtained using the CBM parametrizations, we include a correction on the  $f_{\pi NN}$  coupling constant given by  $f^2 \rightarrow \mathcal{R}f^2$ , as described below. This calibration is necessary in order to obtain a pion cloud contribution to the  $\gamma^*N \rightarrow \Delta$  transition compatible with the experimental data for  $G_M(0)$  [37].

In the covariant spectator quark model, the valence quark contribution to the magnetic form factor at  $Q^2 = 0$  takes the form [37]:

$$G_M^B(0) = \frac{2\sqrt{2}}{3} \frac{1}{3} (2\mu_u + \mu_d), \quad (\text{D24})$$

where the quark effective magnetic moment can be written as

$$\mu_q = \sqrt{\frac{2}{3}} \left[ \frac{2M_B}{M_{B'} + M_B} + \frac{M_B}{M_N} \kappa_q \right] \mathcal{I}(0). \quad (\text{D25})$$

In the previous relation  $\kappa_q$  is the quark anomalous magnetic moment and  $\mathcal{I}(0)$  is the overlap integral of the radial wave functions associated with the  $\gamma^*N \rightarrow \Delta$  transition in the limit  $Q^2 = 0$ .

Equation (D24) is consistent with the CBM result, assuming the exact  $SU(2)$  isospin symmetry, and reproduces also the  $SU(6)$  naive quark model result  $G_M^B(0) = \frac{2\sqrt{2}}{3} \mu_p$ , where  $\mu_p$  is the proton magnetic moment, since  $\mu_p$  can also be represented by  $\bar{\mu}_u$  according to Eq. (C15) [37, 54, 92].

We used the equivalence between the CBM and the covariant spectator quark model results for  $G_M^B(0)$  based on the effective quark magnetic moment  $\mu_q$  to obtain a parametrization of the meson cloud contributions which reproduce the experimental data for the  $\gamma^*N \rightarrow \Delta$  transition. The estimate of the covariant spectator quark model gives a good description of the data for large  $Q^2$  (negligible meson cloud effects). However, to reproduce the low- $Q^2$  data one needs to correct the strength of the meson cloud contribution, regulated by  $f^2/m_\pi^2$ , in order to obtain the correct result for  $Q^2 = 0$ . This calibration is made by determining the necessary factor to reduce the CBM estimate to the covariant spectator quark model estimate for the  $\gamma^*N \rightarrow \Delta$  transition ( $G_M^B(0) \simeq 1.323$ ). One obtains then the factor  $\mathcal{R} = 0.81$  [37]. Notice, however, that the relative contributions from the different meson cloud contributions are still determined by the CBM/SU(6) framework.

The values of  $G_M^{Ka}(0)$  and  $G_M^{Kb}(0)$  presented in Table II are determined using  $\mathcal{R} = 0.81$ .

- 
- [1] I. G. Aznauryan and V. D. Burkert, Prog. Part. Nucl. Phys. **67**, 1 (2012) [arXiv:1109.1720 [hep-ph]].
- [2] G. Ramalho and M. T. Peña, [arXiv:2306.13900 [hep-ph]].
- [3] V. D. Burkert and T. S. H. Lee, Int. J. Mod. Phys. E **13**, 1035 (2004) [nucl-ex/0407020].
- [4] I. G. Aznauryan *et al.*, Int. J. Mod. Phys. E **22**, 1330015 (2013) [arXiv:1212.4891 [nucl-th]].
- [5] D. Drechsel, S. S. Kamalov and L. Tiator, Eur. Phys. J. A **34**, 69 (2007) [arXiv:0710.0306 [nucl-th]].
- [6] V. I. Mokeev *et al.* [CLAS], Few Body Syst. **63**, 59 (2022) [arXiv:2202.04180 [nucl-ex]].
- [7] W. J. Briscoe, M. Doring, H. Habermann, D. M. Manley, M. Naruki, I. I. Strakovsky and E. S. Swanson, Eur. Phys. J. A **51**, 129 (2015) [arXiv:1503.07763 [hep-ph]].
- [8] A. Afanasev *et al.*, Photoproduction of the Very Strangest Baryons on a Proton Target in CLAS12, Report No. JLAB-PR-12-008.
- [9] J. Adamczewski-Musch *et al.* [HADES Collaboration], Phys. Rev. C **95**, 065205 (2017) [arXiv:1703.07840 [nucl-ex]].
- [10] J. Adamczewski-Musch *et al.* [(HADES and PANDA@HADES) Collaborations], Eur. Phys. J. A **57**, 138 (2021).
- [11] P. Cole, B. Ramstein and A. Sarantsev, Few Body Syst. **59**, 144 (2018).
- [12] B. Ramstein [HADES Collaboration], Few Body Syst. **59**, 141 (2018).
- [13] B. Ramstein, Few Body Syst. **59**, 143 (2018); B. Ramstein *et al.* [HADES Collaboration], EPJ Web Conf. **199**, 01008 (2019).
- [14] G. Ramalho, M. T. Peña, J. Weil, H. van Hees and U. Mosel, Phys. Rev. D **93**, 033004 (2016) [arXiv:1512.03764 [hep-ph]].
- [15] G. Ramalho, Phys. Rev. D **102**, 054016 (2020) [arXiv:2002.07280 [hep-ph]].
- [16] J. Adamczewski-Musch *et al.* [HADES], Phys. Rev. C **102**, 024001 (2020) [arXiv:2004.08265 [nucl-ex]].
- [17] J. Adamczewski-Musch *et al.* [HADES], Eur. Phys. J. A **53**, 188 (2017)
- [18] P. Salabura [HADES Collaboration], J. Phys. Conf. Ser. **1643**, 012178 (2020).
- [19] R. Lalik [HADES Collaboration], J. Phys. Conf. Ser. **1137**, 012057 (2019).
- [20] G. Agakishiev *et al.*, Eur. Phys. J. A **50**, 82 (2014) [arXiv:1403.3054 [nucl-ex]].
- [21] R. L. Workman *et al.* [Particle Data Group], PTEP **2022**, 083C01 (2022)
- [22] G. Ramalho and M. T. Peña, Phys. Rev. D **85**, 113014 (2012) [arXiv:1205.2575 [hep-ph]].
- [23] F. Dohrmann *et al.*, Eur. Phys. J. A **45**, 401 (2010) [arXiv:0909.5373 [nucl-ex]].
- [24] R. Abou Yassine *et al.* [HADES], [arXiv:2205.15914 [nucl-ex]].
- [25] G. Ramalho and M. T. Peña, Phys. Rev. D **95**, 014003 (2017) [arXiv:1610.08788 [nucl-th]].
- [26] M. Zétényi, D. Nitt, M. Buballa and T. Galatyuk, Phys. Rev. C **104**, 015201 (2021) [arXiv:2012.07546 [nucl-th]].
- [27] G. Ramalho and M. T. Peña, Phys. Rev. D **101**, 114008 (2020) [arXiv:2003.04850 [hep-ph]].
- [28] J. Kubos *et al.* [HADES Collaboration], J. Phys. Conf. Ser. **1667**, 012023 (2020).
- [29] K. Nowakowski [HADES Collaboration], J. Phys. Conf. Ser. **1667**, 012031 (2020).
- [30] N. Rathod, R. Lalik, A. Malige, P. Salabura and J. Smyrski, Acta Phys. Polon. B **51**, 239 (2020).
- [31] B. Singh [PANDA Collaboration], Nucl. Phys. A **954**, 323 (2016).
- [32] P. Salabura *et al.* [HADES Collaboration], J. Phys. Conf. Ser. **420**, 012013 (2013).
- [33] G. Barucca *et al.* [PANDA Collaboration], Eur. Phys. J. A **57**, 184 (2021) [arXiv:2101.11877 [hep-ex]].
- [34] R. Aaij *et al.* [LHCb], Phys. Lett. B **725**, 25 (2013) [arXiv:1306.2577 [hep-ex]]; R. Aaij *et al.* [LHCb], Phys. Rev. Lett. **120**, 221803 (2018) [arXiv:1712.08606 [hep-ex]].
- [35] M. Ablikim *et al.* [BESIII], Chin. Phys. C **44**, 040001 (2020) [arXiv:1912.05983 [hep-ex]].
- [36] Y. G. Xu, R. M. Wang, X. D. Cheng and Q. Chang, Nucl. Phys. B **977**, 115725 (2022).
- [37] G. Ramalho and K. Tsushima, Phys. Rev. D **88**, 053002 (2013) [arXiv:1307.6840 [hep-ph]].
- [38] J. J. Sakurai, Annals Phys. **11**, 1 (1960).
- [39] G. Feinberg, Phys. Rev. **109**, 1019-1020 (1958)
- [40] M. N. Butler, M. J. Savage and R. P. Springer, Phys. Rev. C **48**, 917 (1993) [nucl-th/9303015].
- [41] R. A. Williams, C. R. Ji and S. R. Cotanch, Phys. Rev. C **48**, 1318 (1993).
- [42] R. Shyam and U. Mosel, Phys. Rev. C **82**, 062201(R) (2010) [arXiv:1006.3873 [hep-ph]].
- [43] M. Zetenyi and G. Wolf, Phys. Rev. C **86**, 065209 (2012) [arXiv:1208.5671 [nucl-th]].
- [44] C. Granados, S. Leupold and E. Perotti, Eur. Phys. J. A **53**, 117 (2017) [arXiv:1701.09130 [hep-ph]].
- [45] O. Junker, S. Leupold, E. Perotti and T. Vitos, Phys. Rev. C **101**, 015206 (2020) [arXiv:1910.07396 [hep-ph]].
- [46] T. Husek and S. Leupold, Eur. Phys. J. C **80**, 218 (2020) [arXiv:1911.02571 [hep-ph]].
- [47] N. Salone and S. Leupold, Eur. Phys. J. A **57**, 183 (2021) [arXiv:2104.05675 [hep-ph]].
- [48] F. Gross, G. Ramalho and M. T. Peña, Phys. Rev. C **77**, 015202 (2008) [nucl-th/0606029].
- [49] G. Ramalho, K. Tsushima and F. Gross, Phys. Rev. D **80**, 033004 (2009) [arXiv:0907.1060 [hep-ph]].
- [50] G. Ramalho, Few Body Syst. **59**, 92 (2018) [arXiv:1801.01476 [hep-ph]].
- [51] R. K. Sahoo, A. R. Panda and A. Nath, Phys. Rev. D **52**, 4099 (1995).
- [52] G. Wagner, A. J. Buchmann and A. Faessler, Phys. Rev. C **58**, 1745 (1998) [nucl-th/9808005].
- [53] R. Bijker, F. Iachello and A. Leviatan, Annals Phys. **284**, 89 (2000) [nucl-th/0004034].
- [54] R. Koniuk and N. Isgur, Phys. Rev. D **21**, 1868 (1980) Erratum: [Phys. Rev. D **23**, 818 (1981)].
- [55] J. W. Darewych, M. Horbatsch and R. Koniuk, Phys. Rev. D **28**, 1125 (1983).

- [56] E. Kaxiras, E. J. Moniz and M. Soyeur, Phys. Rev. D **32**, 695 (1985).
- [57] H. Sanchis-Alepuz, R. Alkofer and C. S. Fischer, Eur. Phys. J. A **54**, 41 (2018) [arXiv:1707.08463 [hep-ph]].
- [58] C. Alexandrou, G. Koutsou, H. Neff, J. W. Negele, W. Schroers and A. Tsapalis, Phys. Rev. D **77**, 085012 (2008) [arXiv:0710.4621 [hep-lat]].
- [59] S. Boinepalli, D. B. Leinweber, P. J. Moran, A. G. Williams, J. M. Zanotti and J. B. Zhang, Phys. Rev. D **80**, 054505 (2009) [arXiv:0902.4046 [hep-lat]].
- [60] T. M. Aliev and A. Ozipineci, Nucl. Phys. B **732**, 291 (2006) [hep-ph/0406331].
- [61] L. Wang and F. X. Lee, Phys. Rev. D **80**, 034003 (2009) [arXiv:0905.1944 [hep-ph]].
- [62] C. L. Schat, C. Gobbi and N. N. Scoccola, Phys. Lett. B **356**, 1 (1995) [hep-ph/9506227].
- [63] J. Y. Kim and H. C. Kim, Eur. Phys. J. C **80**, 1087 (2020) [arXiv:2002.05980 [hep-ph]].
- [64] D. Keller *et al.* [CLAS Collaboration], Phys. Rev. D **85**, 059903 (2012) [arXiv:1111.5444 [nucl-ex]].
- [65] R. M. Wang, X. D. Cheng, Y. Y. Fan, J. L. Zhang and Y. G. Xu, J. Phys. G **48**, 085001 (2021) [arXiv:2008.06624 [hep-ph]].
- [66] M. N. Butler, M. J. Savage and R. P. Springer, Nucl. Phys. B **399**, 69 (1993) [hep-ph/9211247].
- [67] M. Holmberg and S. Leupold, Eur. Phys. J. A **54**, 103 (2018) [arXiv:1802.05168 [hep-ph]].
- [68] R. F. Lebed and R. H. TerBeek, Phys. Rev. D **83**, 016009 (2011) [arXiv:1011.3237 [hep-ph]].
- [69] G. Ramalho, M. T. Peña and F. Gross, Eur. Phys. J. A **36**, 329 (2008) [arXiv:0803.3034 [hep-ph]].
- [70] G. Ramalho, M. T. Peña and F. Gross, Phys. Rev. D **78**, 114017 (2008) [arXiv:0810.4126 [hep-ph]].
- [71] G. Ramalho and M. T. Peña, Phys. Rev. D **80**, 013008 (2009) [arXiv:0901.4310 [hep-ph]].
- [72] G. Ramalho, Phys. Rev. D **95**, 054008 (2017) [arXiv:1612.09555 [hep-ph]]; G. Ramalho, Phys. Rev. D **90**, 033010 (2014) [arXiv:1407.0649 [hep-ph]]; G. Ramalho and K. Tsushima, Phys. Rev. D **89**, 073010 (2014) [arXiv:1402.3234 [hep-ph]].
- [73] G. Ramalho, M. T. Peña and F. Gross, Phys. Rev. D **81**, 113011 (2010) [arXiv:1002.4170 [hep-ph]]; G. Ramalho, M. T. Peña and A. Stadler, Phys. Rev. D **86**, 093022 (2012) [arXiv:1207.4392 [nucl-th]].
- [74] G. Ramalho and K. Tsushima, Phys. Rev. D **84**, 054014 (2011) [arXiv:1107.1791 [hep-ph]].
- [75] G. Ramalho, J. P. B. C. de Melo and K. Tsushima, Phys. Rev. D **100**, 014030 (2019) [arXiv:1902.08844 [hep-ph]].
- [76] G. Ramalho and K. Tsushima, Phys. Rev. D **87**, 093011 (2013) [arXiv:1302.6889 [hep-ph]].
- [77] G. Ramalho and K. Tsushima, Phys. Rev. D **86**, 114030 (2012) [arXiv:1210.7465 [hep-ph]].
- [78] G. Ramalho, D. Jido and K. Tsushima, Phys. Rev. D **85**, 093014 (2012) [arXiv:1202.2299 [hep-ph]].
- [79] G. Ramalho, M. T. Peña and K. Tsushima, Phys. Rev. D **101**, 014014 (2020) [arXiv:1908.04864 [hep-ph]].
- [80] G. Ramalho, Phys. Rev. D **103**, 074018 (2021) [arXiv:2012.11710 [hep-ph]].
- [81] F. Gross, G. Ramalho and M. T. Peña, Phys. Rev. D **85**, 093006 (2012) [arXiv:1201.6337 [hep-ph]].
- [82] G. Ramalho and K. Tsushima, Phys. Rev. D **94**, 014001 (2016) [arXiv:1512.01167 [hep-ph]].
- [83] M. I. Krivoruchenko and A. Faessler, Phys. Rev. D **65**, 017502 (2001) [arXiv:nucl-th/0104045].
- [84] H. F. Jones and M. D. Scadron, Annals Phys. **81**, 1 (1973).
- [85] R. C. E. Devenish, T. S. Eisenschitz and J. G. Korner, Phys. Rev. D **14**, 3063 (1976).
- [86] G. Wolf, G. Batko, W. Cassing, U. Mosel, K. Niita and M. Schaefer, Nucl. Phys. A **517**, 615 (1990).
- [87] G. Ramalho, Phys. Rev. D **100**, 114014 (2019) [arXiv:1909.00013 [hep-ph]].
- [88] G. Ramalho, Eur. Phys. J. A **54**, 75 (2018) [arXiv:1709.07412 [hep-ph]].
- [89] G. Ramalho, Phys. Rev. D **94**, 114001 (2016) [arXiv:1606.03042 [hep-ph]].
- [90] F. Gross, Phys. Rev. **186**, 1448 (1969); A. Stadler, F. Gross and M. Frank, Phys. Rev. C **56**, 2396 (1997) [arXiv:nucl-th/9703043].
- [91] F. Gross, G. Ramalho and M. T. Peña, Phys. Rev. D **85**, 093005 (2012) [arXiv:1201.6336 [hep-ph]].
- [92] V. Pascalutsa, M. Vanderhaeghen and S. N. Yang, Phys. Rept. **437**, 125 (2007) [hep-ph/0609004].
- [93] L. Tiator, D. Drechsel, O. Hanstein, S. S. Kamalov and S. N. Yang, Nucl. Phys. A **689**, 205 (2001) [nucl-th/0012046].
- [94] C. Becchi and G. Morpurgo, Phys. Lett. **17**, 352 (1965).
- [95] S. L. Glashow, Physica A **96** 1, 27 (1979).
- [96] N. Isgur, G. Karl and R. Koniuk, Phys. Rev. D **25**, 2394 (1982).
- [97] M. I. Krivoruchenko and M. M. Giannini, Phys. Rev. D **43**, 3763 (1991).
- [98] B. Julia-Diaz, T.-S. H. Lee, T. Sato and L. C. Smith, Phys. Rev. C **75**, 015205 (2007) [nucl-th/0611033].
- [99] S. J. Brodsky and G. R. Farrar, Phys. Rev. D **11**, 1309 (1975).
- [100] C. E. Carlson and N. C. Mukhopadhyay, Phys. Rev. Lett. **81**, 2646 (1998) [hep-ph/9804356]; C. E. Carlson, Phys. Rev. D **34**, 2704 (1986); C. E. Carlson, Few Body Syst. Suppl. **11**, 10 (1999) [hep-ph/9809595].
- [101] P. A. Carruthers, *Introduction to unitary symmetry*, Interscience Publishers (New York) 1966.
- [102] A. W. Thomas, Adv. Nucl. Phys. **13**, 1 (1984).
- [103] S. Theberge and A. W. Thomas, Nucl. Phys. A **393**, 252 (1983).
- [104] K. Kubodera, Y. Kohyama, K. Oikawa and C. W. Kim, Nucl. Phys. A **439**, 695 (1985).
- [105] K. Tsushima, T. Yamaguchi, Y. Kohyama and K. Kubodera, Nucl. Phys. A **489**, 557 (1988).
- [106] T. Yamaguchi, K. Tsushima, Y. Kohyama and K. Kubodera, Nucl. Phys. A **500**, 429 (1989).
- [107] D. H. Lu, A. W. Thomas and A. G. Williams, Phys. Rev. C **57**, 2628 (1998) [nucl-th/9706019].
- [108] D. H. Lu, A. W. Thomas and A. G. Williams, Phys. Rev. C **55**, 3108 (1997) [nucl-th/9612017].
- [109] G. Kalbermann and J. M. Eisenberg, Phys. Rev. D **28**, 71 (1983).
- [110] K. Bermuth, D. Drechsel, L. Tiator and J. B. Seaborn, Phys. Rev. D **37**, 89 (1988).
- [111] H. B. O'Connell, B. C. Pearce, A. W. Thomas and A. G. Williams, Phys. Lett. B **354**, 14 (1995) [hep-ph/9503332].
- [112] H. B. O'Connell, B. C. Pearce, A. W. Thomas and A. G. Williams, Prog. Part. Nucl. Phys. **39**, 201 (1997) [hep-ph/9501251].
- [113] H. C. Donges, M. Schafer and U. Mosel, Phys. Rev. C **51**, 950 (1995) [nucl-th/9407012].

- [114] G. J. Gounaris and J. J. Sakurai, *Phys. Rev. Lett.* **21**, 244 (1968).
- [115] L. M. Barkov *et al.*, *Nucl. Phys. B* **256**, 365 (1985).
- [116] M. Herrmann, B. L. Friman and W. Norenberg, *Nucl. Phys. A* **560**, 411 (1993).
- [117] M. Benayoun, M. Feindt, M. Girone, A. Kirk, P. Leruste, J. L. Narjoux and K. Safarik, *Z. Phys. C* **58**, 31 (1993).
- [118] J. D. Jackson, *Nuovo Cim.* **34**, 1644 (1964).
- [119] Section properties of  $\rho(770)$  in Ref. [21].
- [120] J. Pisut and M. Roos, *Nucl. Phys. B* **6**, 325 (1968).
- [121] K. Nakamura *et al.* [Particle Data Group], *J. Phys. G* **37**, 075021 (2010).
- [122] D. Keller *et al.* [CLAS Collaboration], *Phys. Rev. D* **83**, 072004 (2011) [arXiv:1103.5701 [nucl-ex]].
- [123] J. Colas, C. Farwell, A. Ferrer and J. Six, *Nucl. Phys. B* **91**, 253 (1975).
- [124] V. V. Molchanov *et al.* [SELEX Collaboration], *Phys. Lett. B* **590**, 161 (2004) [hep-ex/0402026].
- [125] M. Ablikim *et al.*, *Phys. Rev. D* **101**, 012004 (2020) [arXiv:1911.06669 [hep-ex]].
- [126] P. Mühlich and U. Mosel, *Nucl. Phys. A* **773**, 156 (2006) [nucl-th/0602054]; P. Mühlich, Ph. D. thesis, University of Giessen, 2007.
- [127] S. R. Amendolia *et al.* [NA7 Collaboration], *Nucl. Phys. B* **277**, 168 (1986); C. N. Brown *et al.*, *Phys. Rev. D* **8**, 92 (1973); C. J. Bebek *et al.*, *Phys. Rev. D* **9**, 1229 (1974); C. J. Bebek, C. N. Brown, M. Herzlinger, S. D. Holmes, C. A. Lichtenstein, F. M. Pipkin, S. Raither and L. K. Sisterson, *Phys. Rev. D* **13**, 25 (1976); C. J. Bebek *et al.*, *Phys. Rev. D* **17**, 1693 (1978); G. M. Huber *et al.* [Jefferson Lab Collaboration], *Phys. Rev. C* **78**, 045203 (2008) [arXiv:0809.3052 [nucl-ex]].
- [128] A. D. Bukin *et al.*, *Phys. Lett. B* **73**, 226 (1978); A. Quenzer *et al.*, *Phys. Lett. B* **76**, 512 (1978); L. M. Barkov *et al.*, *Nucl. Phys. B* **256**, 365 (1985); R. R. Akhmetshin *et al.* [CMD-2 Collaboration], *Phys. Lett. B* **527**, 161 (2002) [hep-ex/0112031]; R. R. Akhmetshin *et al.* [CMD-2 Collaboration], *Phys. Lett. B* **648**, 28 (2007) [hep-ex/0610021]; M. N. Achasov *et al.*, *J. Exp. Theor. Phys.* **101**, 1053 (2005) [Zh. Eksp. Teor. Fiz. **128**, 1201 (2005)] [hep-ex/0506076].
- [129] W. Bartel, B. Dudelzak, H. Krehbiel, J. McElroy, U. Meyer-Berkhout, W. Schmidt, V. Walther and G. Weber, *Phys. Lett. B* **28**, 148 (1968); S. Stein *et al.*, *Phys. Rev. D* **12**, 1884 (1975).